Experimental and Numerical Investigation of the Erosive Effects of Micro- and Nanometer-Sized Particles in Water Flow

by
Marthe Braut

Master of Science in Process Technology
Specialization in Multiphase Systems

Department of Physics and Technology
University of Bergen

June 2020

Abstract

The demand for efficient and sustainable energy is continuously increasing. Among the many technologies with great potential within this field are *nanofluids*. Their enhanced heat transfer properties make them a great replacement to original working fluids in heat transfer and thermal storage systems. This has the potential to improve such systems, thus increasing the efficiency and lowering the costs. Yet, there is still a considerable lack of information regarding their erosive and corrosive effects on systems materials. The key factors and their level of influence on erosion need to be established before applying nanofluids to larger industrial systems.

The objective of the present work is to investigate the erosive effects of liquids containing small, suspended particles, using both experimental and numerical methods.

For the experimental work, the tribological behavior of aqueous 1.33 wt.% TiO_2 nanofluid was investigated when jet-impinged at flat targets of various materials. Further, erosion was found by assessing the target surfaces using scanning electron microscopy (SEM) and weight differences of the targets. It was found that impinging TiO_2 nanofluid caused mass losses for plastic targets and copper targets, with mass loss rates of 0.144 g/year and 0.186 g/year, respectively. A resulting mass gain was found for rubber targets. The wear of the copper targets was considered as the result of an erosion-corrosion process.

Furthermore, a static light scattering analysis of the nanofluid was conducted to investigate how its stability changes over a test duration of 336 hours. A range of smaller sizes was detected for the nanofluid after the experiment compared to before its start. This can be explained by the settling of the largest particles, in addition to the possible breaking of agglomerates due to circulation.

Additionally, a numerical investigation was done using the computational fluid dynamics (CFD) software STAR-CCM+. This computational tool studied the erosive effect of micrometer-sized particles dispersed in a fluid stream for a similar geometry as the experimental one. The particles were tracked by the Langrangian approach. The erosion rate was examined by alterations in injector velocity, dispersed particle density, and particle diameter. Enhancement in velocity and density caused an increased erosion rate, while a critical diameter was revealed for the diameter-based simulations. At this diameter, we experience a minimum erosion rate (at $4.593 \cdot 10^{-6}$ g/year), in addition to a shift in the location of the erosion field. Nonetheless, it is important to note that such small rates are not entirely representative due to numerical errors.

From this research, it is evident that erosion is a complex phenomenon. The simulations detected injector velocity, dispersed particle density, and particle diameter as significant factors for the erosion rate. Especially particle diameter was identified as a critical parameter. The experimental work was not able to establish any key factors, and the erosion rates were found to be of low values. To summarize, erosion is a result of numerous factors, and one needs to investigate the specific nanofluid-system material combination before applying a nanofluid to a system.

Acknowledgements

Foremost, I would like to express my gratitude to my supervisor, professor Pawel Kosinski at the University of Bergen for his guidance and help throughout this master thesis. A special thanks for his assistance in STAR-CCM+. Furthermore, I would like to thank my co-supervisor, professor Boris V. Balakin at the Western Norway University of Applied Sciences for his expertise on the subject, for being very helpful with planning the experiment, and for taking the time to help me solve problems related to the experimental set-up.

I would also like to thank Senior Engineer Harald Moen at Western Norway University of Applied Sciences for developing and manufacturing the experimental set-up, and for further help throughout the semester. A sincere thanks to Irene Heggstad at ELMIlab for the help in obtaining the SEM images, and for her excellent explanations.

Thanks are also necessary for Halvard Thon, who has helped with general guidance in thesis writing, in addition to sharing his knowledge about using nanofluids in the Malvern Mastersizer 2000. A special thanks for providing a SEM image of dry TiO_2 particles.

I wish to thank my fellow master students at the Department of Physics and Technology for many pleasant conversations and the sharing of numerous cups of coffee. A special thanks to Lisbeth Espedal, Mattias Stava, Runa By Bårdsgård, and Njål Frafjord for a great year in the "multiphase"-office. Finally, I would like to express my sincere appreciation to my family and friends for their love and support during this period.

Nomenclature

Abbreviations

CFD	Computational Fluid Dynamics
DEM	Discrete Element Method
DPM	Discrete Parcel Method
E-E	Eulerian-Eulerian
NF	Nanofluid
NP	Nanoparticle
NS	Navier-Stokes
PDE	Partial Differential Equation
PSD	Particle Size Distribution
PVC	Polyvinyl Chloride
PVP	Polyvinylpyrrolidone
RANS	Reynolds Averaged Navier-Stokes
SEM	Scanning Electron Microscope
SLS	Static Light Scattering
SSA	Specific Surface Area
SST	Shear Stress Transport

Greek Symbols

α	Volume fraction	[-]
μ	Dynamic viscosity	[Pa·s]
ν	Kinematic viscosity	$[m^2/s]$
ω	Specific dissipation rate	$[s^{-1}]$
ϕ	Scattering angle	[-]

ρ	Density	[kg/m^3]
τ	Shear stress	[Pa]
θ	Impact angle	[-]

Latin Letters

A	Reference area	[m^2]
a	Acceleration	[m/s^2]
C_D	Drag coefficient	[-]
D	Diameter	[m]
D_p	Particle diameter	[m]
D'	User-specified reference diameter	[m]
e	Restitution coefficient	[-]
E_{90}	Erosion damage at normal impact angle	[mm^3/kg]
ER	Volumetric erosion damage	[mm^3/kg]
F_D	Drag force	[N]
Hv	Vickers hardness	[N/m^2]
k	Kinetic energy	[J]
m	Mass	[kg]
$\dot{m}$	Mass flow rate	[kg/s]
M$_d$	Total mass of the dispersed phase	[kg]
M$_{total}$	Total mass	[kg]
q	Absolute intensity	[W/m^2]
$\dot{Q}$	Volume flow rate	[m^3/h]
Re	Reynolds number	[-]
u*	Reference velocity	[m/s]
u$^+$	Non-dimensional velocity	[-]
V	Velocity	[m/s]
ΔV_d	Total volume of the dispersed phase within a domain Δ	[m^3]
ΔV	Total volume within a domain Δ	[m^3]
V'	User-specified reference speed	[m/s]
V$_0$	Inlet velocity	m/s

V_p	Particle impact speed	[m/s]
W_m	Mass fraction	[-]
y	Wall-normal distance	[m]
y^+	Non-dimensional wall distance	[-]
$\mathbf{F}$	Force vector	[N]
$\mathbf{V}$	Velocity vector	[m/s]

Subscripts

c	Continuous phase
d	Dispersed phase
m	Mixture
p	Particle
t	Turbulent
w	Wall

Contents

List of Figures

List of Tables

Chapter 1

Introduction

The global energy demand is continuously growing, with a worldwide primary energy consumption increasing with 2.9% in 2018 [8]. Consumers are becoming more conscious about energy sources and their production, especially when it comes to their impact on the global environment. Although the population of the first world is involved in the environmental impact of energy consumption, there are still unresolved problems when it comes to energy access in third world countries. There are yet numerous energy-related challenges to be solved, and the development of efficient and sustainable energy supply is more urgent than ever.

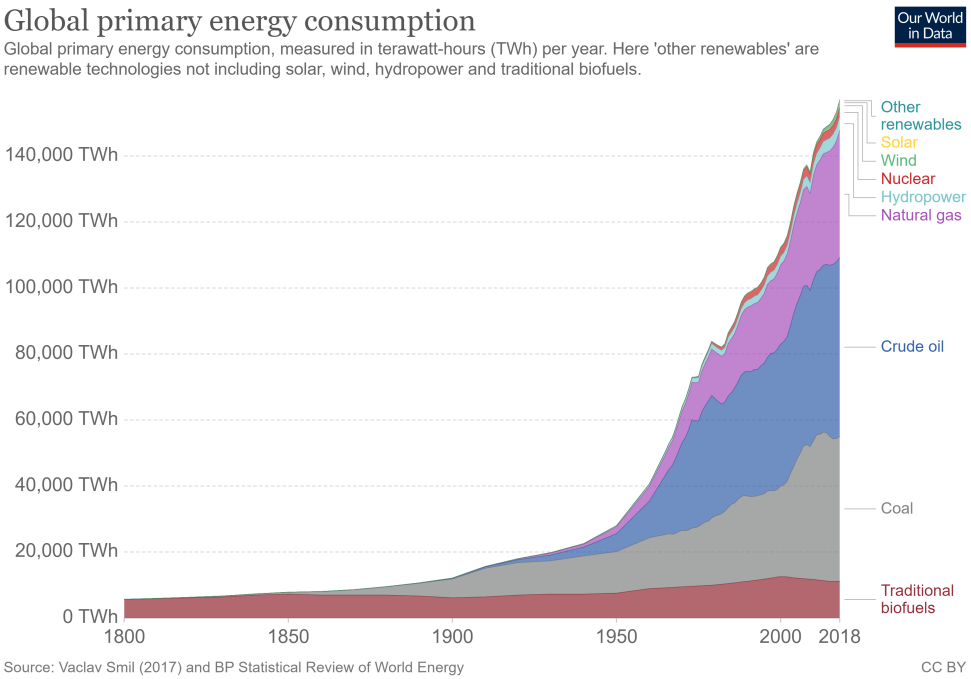

Figure 1.1: Global primary energy consumption [8][51][73].

The annual worldwide primary energy consumption in 2018 was 157 000 TwH [8]. It is difficult to put these enormous amounts of energy into perspective. To illustrate, this amount of energy equals the energy released from the Hiroshima nuclear bomb every four seconds.

Historical and current energy systems are dominated by fossil fuels (as seen in Figure 1.1), which emit carbon dioxide CO_2 and other greenhouse gases: the major contributors to global warming. Although a change from fossil-fuel based energy to a low-carbon one has been of important focus the last decades, it has been a slow transition so far. The main global energy source remains fossil fuels, constituting 85% of the world's energy consumption. There is a need of evolving our current energy systems into more sustainable and efficient ones.

A new research area that has great potential in this field is *nanofluids*. Nanofluids are nanometer-sized particles dispersed in a base fluid such as water or oil. The added particles alter the chemical and physical properties of the base fluid, and the properties of most interest are the heat transfer properties. Their thermal properties have attracted a lot of attention to the field of nanofluids.

The presence of solid particles in the fluid enhances heat transfer, which again causes a significant improvement in terms of efficiency and economy when applied to energy systems. The application studied most intensively up to this point is their role as heat transfer fluids in solar collectors. Their application in various energy systems such as heat exchangers, radiators, and cooling systems has also been explored.

Despite the very interesting advantages of the possible application of nanofluids, there are major drawbacks with solid particles dispersed in operating fluids. Although nanoparticles are of significantly small size, they have the potential to cause wear of surrounding material (see Figure 1.2). Thus, there is a need to identify the tribological behavior of nanofluids before use in large industrial applications. Additionally, the performance of nanofluids is strongly connected to their stability, and the agglomeration of nanoparticles is a common problem in the manufacturing and application of nanofluids.

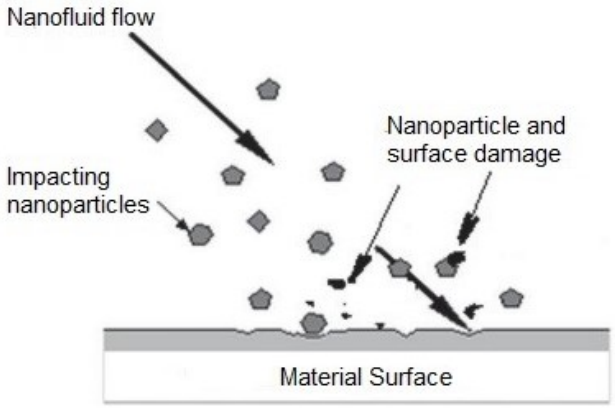

Figure 1.2: Schematic of erosion due to nanofluid flow over material surface.

The erosive effects of nanofluids have been investigated for over 10 years, but there is still a need for further investigation to understand the interaction between a working nanofluid and its surrounding material.

Many mathematical models have been developed with an objective to precisely predict the erosion rate of solid particles in a fluid flow, for instance, Oka et al. [50] and DNV GL [79]. However, there are several challenges when finding an accurate model, as many parameters are affecting the erosion rate, such as impact speed, impact angle, particle concentration, and target material. With recent advantages in software technologies, the application of CFD (Computational Fluid Dynamics) to predict erosion in industrial processes has become possible. CFD is a cost-effective and time-saving tool for erosion prediction and has been used extensively for multiple applications, e.g. sand erosion in oil- and gas pipelines. CFD has the potential to predict both the location and magnitude of erosion caused by nanofluid flow, however, its applicability and accuracy are yet to be established.

1.1 Specific Objectives

The objective of this thesis is to investigate the erosion damage caused by nano- and micrometer-sized particles suspended in an impinging fluid, both by experimental and numerical methods.

The specific objectives of this thesis were to:
(i) build and optimize an experimental laboratory set-up
(ii) study the effects of erosion by TiO_2/water nanofluid of various materials in the set-up
(iii) simulate erosion by micrometer-sized particles in water flow in the commercial CFD-software STAR-CCM+, namely:

- the effect of particle size
- the effect of velocity
- the effect of material properties

Chapter 2

General Theory

The following chapter introduces the relevant background theory for this work.
In the first section, the topic of erosion and its mechanisms are introduced, followed by a presentation of nanofluids. Next, a section elaborates CFD; namely its physical basis and applications. Finally, some important parameters to characterize multiphase flows by are explained.

2.1 Erosion

Erosion is known as the mechanical wear of a solid surface, caused by impinging particles suspended in a flow (liquid, gas, or multiphase). In other words, it can be described as particles continuously striking a surface, causing removal and deformation of surface material.

Erosion types can be classified into two mechanisms: impact erosion and abrasive erosion. Abrasive erosion is caused by hard particles sliding, rolling or jumping along a surface, causing wall material to be cut off. Impact erosion occurs at a larger impact angle and causes wall material to deform or to be displaced [41].

Whether the occurring wear mechanism is impact erosion or abrasive erosion is also determined by other factors, e.g. if the wall material is brittle or ductile. When a particle hits the surface of a ductile material, it can either cause deformation or surface fatigue. The process highly depends on impact angle, velocity, and surface material property. For ductile materials, the erosion rate is most severe for low impact angles, while for brittle materials, erosion rate is largest at high impact angles [17][22], as shown in Figure 2.1.

Erosion wear can be expressed in various terms, but the most common is *erosion rate*. Erosion rate is defined as the surface material mass loss per unit area per unit time. Many mathematical models have been developed in order to express erosion rate in terms of various parameters such as impact velocity, particle size, and impact angle. This topic is further elaborated in Chapter 3.5.

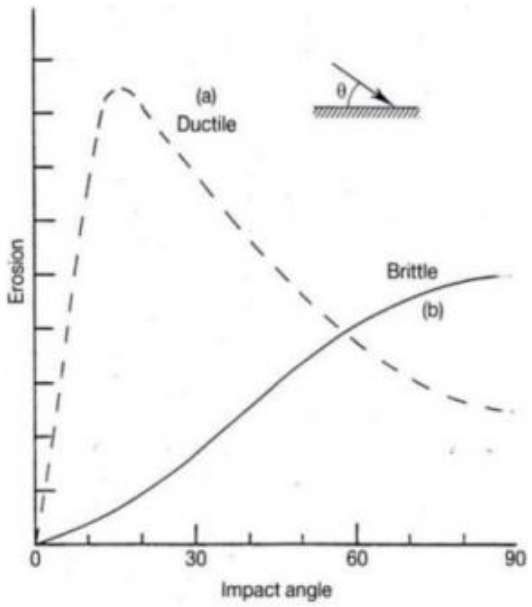

Figure 2.1: The influence of impact angle θ on the erosion (dimensionless) for (a) ductile and (b) brittle materials [32].

2.2 Nanofluids

Nanofluids (NF) are two-phase systems consisting of dispersed nanoscale materials (nanoparticles, nanosheets, nanofibers, nanotubes, nanorods, nanowires, or nanodroplets) in base fluids [87]. The term was first proposed by Choi et al. [13] in 1995. NFs are found to possess multiple improved properties compared to their base fluids, such as increased stability, viscosity, thermal diffusivity, thermal conductivity [26][52] and convective heat transfer coefficients [27][87]. These enhanced properties make them desirable for heat transfer applications such as heat exchangers and cooling systems.

The NF property of most interest is the thermal conductivity, and it is shown to increase by up to 30 % compared to base fluids [85]. The smaller particles result in an increased specific surface area (SSA), leading to more interactions among nanoparticles (NP), and amongst base fluid molecules and NP's. The larger SSA also stabilizes the suspensions due to the Brownian motion of the particles [37][82].

Nonetheless, agglomeration is a common challenge when manufacturing NF's. NP's dispersed in liquids tend to agglomerate due to their nanoscale size and high surface energy, which minimizes the suspension's stability and thus its thermal and optical properties [60]. The addition of surfactants has proved to be an easy and cheap method to minimize agglomeration [65][68]. Ultrasonicating baths, probe ultrasonication, mechanical stirring, and magnetic stirring are additional tools that apply mechanical energy to the fluid in order to disperse the nanoparticles.

NP's used in NF's can vary between metallic, non-metallic and carbon-based particles. Of

the carbon-based nanofluids, particles such as such as carbon-black (CB), graphene [67] and carbon nanotubes (e.g. single-, double- and multi-walled carbon nanotubes [4][14]) have been used. Metallic NP's are also used: iron (Fe)[29], copper (Cu)[19][86], gold (Au)[53], and silver (Ag)[53]. At last, there are also non-metallic NP's which are usually oxides, such as aluminium oxide (alumina)[12], titanium dioxide [12] and iron oxide [7][31][55]. The base liquids most commonly used for NF manufacturing are water, glycols [11] and thermal oils (e.g. Therminol VP1 and Syltherm 800) [7][46].

There exist two main categories for the preparation of NF's, namely two-step methods and one-step methods. The most common, often due to their economic benefits when produced in large quantities, are the two-step methods. Nanometer-sized material is first produced as a dry powder, which is further dissolved in a fluid. Finally, the mixture is treated with either mixing, magnetic force agitation, and/or ultrasonic agitation. One drawback of these methods is their difficulty with producing stable NF's without agglomerates. In the other method (one-step), NP's are simultaneously synthesized and dispersed in the fluid. Examples of such methods are physical vapor deposition, inert gas condensation, and chemical reduction [54][89]. For most preparations, two-step methods will be sufficient as one-step methods are more costly.

2.3 Computational Fluid Dynamics

Computational fluid dynamics (CFD) is the application of algorithms and numerical techniques to solve fluid flow phenomena [80]. In more detail, it is the study of fluid flow through numerical simulations, which involves employing computer programs or software packages performed on high-speed digital computers to attain numerical solutions. The computers perform repetitive manipulation of enormous amounts of numbers. Yet, it is important to note that CFD provides predictive and approximated solutions. CFD has become a powerful tool for use in research or industrial application.
The CFD software applied in this thesis is Siemens STAR CCM+ version 13.06.012-R8. STAR CCM+ provides tools for creating complex geometries and mesh, applying boundary conditions and setting up physical models, and finally obtaining a simulation result for fluid flow under real-world conditions.

2.3.1 The Governing Equations of CFD

CFD is based on the fundamental conservation laws of fluid dynamics: the continuity, momentum, and energy equations. They are the mathematical statements of the physical principles which all of fluid dynamics is based on:

1. Mass is conserved
2. Newton's second law, $\mathbf{F} = \mathbf{ma}$
3. Energy is conserved

These physical principles can be expressed as basic mathematical equations which are integral equations or partial differential equations (PDE). CFD is based on the replacement of the integrals or derivatives with discretized algebraic forms, which in turn are solved to obtain numbers for the flow field values at discrete points in time and/or space. Thus, the product of CFD is a collection of numbers, compared to a closed-form analytical solution.

As previously stated, the mathematical equations can be obtained as both integral or PDE's in conservative or non-conservative forms. The PDE's follow infinitesimally small elements, while integral equations follow control volumes. In both cases, the elements can be fixed in space or move with the flow. This results in four models of flow. The conservation form equations follow an element fixed in space, and non-conservation form equations follow an element moving with the flow.

A term necessary to introduce to describe the fluid dynamics is the *substantial* derivative. It applies to any flow-field variable, such as pressure, density, and temperature. The substantial derivate is given by $\frac{D}{Dt}$. It represents the instantaneous time rate of change following a moving fluid element. Its relevance is due to the model selected: infinitesimal fluid element moving with the flow, as illustrated in Figure 2.2. The model selected will provide PDE's in non-conservation form.

Compared to the *local derivative* $\frac{\partial}{\partial t}$ which is the time rate at a fixed point, the substantial derivative follows a moving fluid element. The substantial derivative combines both local

and convective derivative, and thus becomes a total derivative with respect to time:

$$\frac{D}{Dt} \equiv \frac{\partial}{\partial t} + (\boldsymbol{V} \cdot \nabla), \tag{2.1}$$

where $\boldsymbol{V} \cdot \nabla$ is the *convective derivative* which is physically the time rate of change of the volume of a moving fluid element per unit volume [2].

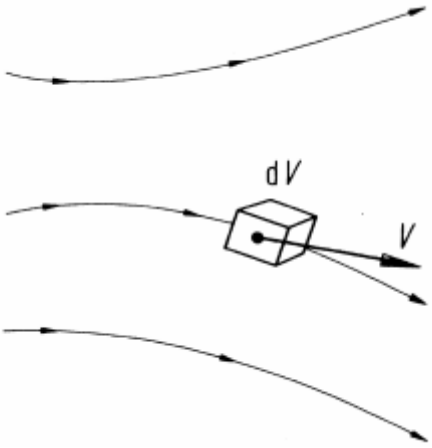

Figure 2.2: Infinitesimal fluid element moving along a streamline with the velocity V equal to the local flow velocity at each point [2].

To obtain a representative equation for a given fluid flow phenomenon, one needs to: (1) select a physical principle, (2) apply it to a model of the flow, and (3) derive an equation that represents the fluid flow.

The **continuity equation** origins in the physical principle *Mass is conserved*:

$$\frac{D\rho}{Dt} + \rho \nabla \cdot \boldsymbol{V} = 0. \tag{2.2}$$

The **momentum equation** is based on the physical principle $\mathbf{F} = m\mathbf{a}$

When considering this relation, it says that a moving fluid element experiences a net force which is equal to its mass times the acceleration of the element. This force can be divided into three relations along the x, y, and z axes. Along each direction, there are only two forces acting on the moving fluid element. They origin from:

1. *Body forces*, which act directly on the volumetric mass of the fluid element. These forces "act at a distance", e.g. gravitational, electric, and magnetic forces.

2. *Surface forces*, which act directly on the surface of the fluid element. They are due to two sources:

- The pressure distribution acting on the surface, imposed by the outside fluid
- The shear and normal stress distributions acting on the surface imposed by the outside fluid (by means of friction)

Both surface forces are imposed by the outside fluid.

The momentum increment of the fluid flow per unit time equals the sum of the body forces and the surface forces acting on the moving fluid element. A short definition of the momentum equation is:

$$\rho\frac{Du}{Dt} = -\frac{\partial p}{\partial x} + \frac{\partial \tau_{xx}}{\partial x} + \frac{\partial \tau_{yx}}{\partial y} + \frac{\partial \tau_{zx}}{\partial z} + \rho f_x, \tag{2.3}$$

where τ_{xx}, τ_{yx}, τ_{zx} are the normal and shear stresses in the x-direction exerted on a plane perpendicular to the x, y and z axis, respectively. The first term on the right-hand-side of the equation expresses pressure forces. The last term describes a body force.

Note that Equation (2.3) is the x-component of the momentum equations.

The **energy equation** comes from the application of the energy conservation principle, which also is the first law of thermodynamics. When applied to a flow model of a moving fluid element it states that the rate of change of energy inside the fluid element equals the net heat flux into element plus the rate of work done on the element due to body and surface forces [2].

The energy equation was not used in this thesis.

2.3.2 Physical Boundary and Initial Conditions

The governing equations are the same for several flow phenomena, but they need to be defined for each studied flow field. This is where boundary conditions need to be introduced. Boundary conditions dictate the particular solutions to be obtained from the governing equations. Hence, the boundary condition is the real driver for any particular solution. In the case of viscous flow, one can assume zero relative velocity between the surface and the liquid particles immediately at the surface. This is called the *no-slip* condition. Also, if the surface is stationary with the flow moving past it, then (at the surface):

$$u = v = w = 0, \tag{2.4}$$

where u, v and w are velocities in the x-, y- and z-direction, respectively.

The boundary conditions are applied in each time step. On the other hand, the initial conditions define the starting solution of the whole domain, and they are replaced as soon as the solver starts to run. The boundary and initial conditions used in the model are described in Chapter 4.

2.3.3 Discretization and Mesh

The governing equations explain the flow-field in terms of PDE's. Analytical solutions of PDE's involve closed-form expression yielding variation of dependent variables continuously throughout the domain. By discretization of the equations, a numerical solution is achieved, providing answers at a finite amount of grid points, and at a certain amount of time-steps.

Anderson [2] describes discretization as the process by which a closed-form mathematical expression, such as a function or a differential or integral equation involving functions, all of which are viewed as having an infinite continuum of values throughout some domain, is approximated by analogous expressions which prescribe values at only a finite number of discrete points or volumes in the domain

The discretization of CFD can be classified into mesh methods and mesh-free methods, or preferably structured or unstructured. The former are most common, and are based on the Eulerian approach (further elaborated in section 2.5.2). Mesh-free methods are on the other hand rarely used as they cost extra programming time and computational effort. The absence of a mesh allows for Langrangian simulation. These include smooth particle hydrodynamics and finite pointset method.

For Eulerian approaches, discretization starts with breaking down the domain into smaller regions or cells, whose vertices are called nodes (grid points). The arrangement of these discrete points throughout the flow field is called a grid. Appropriate grids or meshes need to be established, and equations solved over these grids. Further, the governing equations are discretized over the mesh. All CFD methods utilize some form of discretization, and the most common is the finite-difference approach. The two others are called finite volume and finite elements and have been used for computational mechanics over several years. Yet, the finite difference method is the main technique today.

Finite-difference solutions are widely employed in CFD and are based on the replacement of partial derivatives in the governing equations by approximate algebraic difference quotients. This yields a system that can be solved for the values of the flow-field variables at discrete points only. The most common finite-difference representations of derivatives are based on Taylor's series expansions.

There exist two main categories for CFD techniques used to solve transient equations originated from the finite-difference method:

1. *The explicit approaches*, where each difference equation contains only one unknown and therefore can be solved straightforwardly.

2. *The implicit approaches*, where the unknowns must be obtained through a simultaneous solution of the difference equations applied at all the grid points arrayed at a given time level.

The approach selected in this thesis is the implicit approach, which is beneficial due to its ability to maintain stability over large values of Δt (time step).

2.4 Multiphase Systems

A multiphase system is a system with the simultaneous presence of several phases, i.e. liquid, vapor, or solid. It consists of one or more dispersed phases in one or more continuous phases. Examples are gas-liquid transportation, crude oil recovery, and air pollution. The most common are two-phase systems, consisting of one dispersed phase in one continuous phase. Dispersed two-phase flows are flows of particles or droplets, i.e. the dispersed phase, where the dispersed phase is not materially connected. The surrounding fluid is a continuum, meaning its density and velocity vary continuously from point to point.

2.4.1 Characterization of Two-Phase Flows

For the characterization of two-phase flows, multiple properties need to be defined. To begin with, the volume fraction is the fraction of the volume occupied by the dispersed phase per unit volume. Hence, the volume fraction α_d is given by:

$$\alpha_d = \frac{\Delta V_d}{\Delta V}, \tag{2.5}$$

where ΔV_d is the volume occupied by the dispersed phase. Another suitable measure of the concentration is the mass fraction, W_m:

$$W_m = \frac{\text{mass of dispersed phase}}{\text{total mass}} = \frac{M_d}{M_{total}}, \tag{2.6}$$

which is the ratio of the mass of the dispersed phase to that of the continuous phase in a mixture. There exists several other terms related to the concentration of the fluid, but volume fraction (α_d) and mass fraction (W_m) are most relevant for this work.

Two-phase flows can also be classified as dense or dilute flows. A dilute dispersed phase flow is one in which the particle motion is controlled by fluid forces, e.g. drag and lift. A dense flow is on the other hand one in which the particle motion is controlled by collisions or continuous contact [17].

An additional important concept to characterize multiphase flows by is phase coupling. When there is more than one phase present in a flow, these phases can affect each other. The flow is said to be *one-way coupled* if one phase affects the other but it does not happen in return. If the two phases affect one another the flow is so-called *two-way coupled*.

Finally, the concept of response times needs to be defined. Response time is the time it takes a particle or droplet to respond to a change in temperature or velocity. Hence there are two terms: the *thermal response time* and the *momentum (velocity) response time*. Per definition, the response time is the time it takes for a particle released from rest to achieve 63% of the velocity/temperature of the carrier fluid [17].

2.5 Numerical Modeling of Multiphase Flows

Many approaches are found in the literature for modeling multiphase flows. Compared to single-phase flows, the numerical methods and modelings for multiphase flows are much more challenging but less mature. The field remains one of the most active areas in CFD. An ideal numerical model for the dispersed phase would resolve the dynamics and thermal properties of all particles in the system. The large amount of particles in industrial applications causes this method to be unattainable. Thus, rather than following each particle, the *particle cloud approach* is applied, meaning that "bulk" properties are identified and interpreted in terms of mixing, chemical reactions, and other processes.

Approaches for modeling two-phase flows can be categorized into Eulerian-Eulerian and Eulerian-Langrangian, as illustrated in Figure 2.3. The two approaches are both widely used in the computation of macroscopic two-phase flows. The continuous phase is in both approaches resolved by Eulerian modeling, meaning that the Navier-Stokes (NS) equations are solved for the fluid flow. Their differences lie in how they treat the dispersed phase.

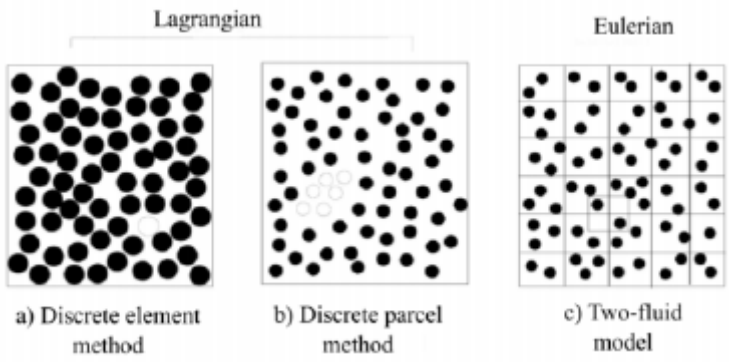

Figure 2.3: Three approaches for numerical simulation of two-phase flow: a) Discrete Element Model b) Discrete Parcel Method c) E-E (two-fluid model) [17].

2.5.1 Eulerian-Eulerian

In the **Eulerian model**, the dispersed particles are described as a continuous fluid, resulting in it commonly being referred to as the *two-fluid model*. Equations are developed for the average properties of the particles or droplets in the cloud. Differential conservation equations are written for every node in the grid, which are discretized and the solution of the resulting set of algebraic equations gives the properties of the cloud. The equations of the dispersed phase can be treated with the same discretization and similar numerical techniques as those used for the continuous phase, making the process computationally efficient.

2.5.2 Eulerian-Lagrangian

As shown in Figure 2.3, there exist two Langrangian models, namely the Discrete Element Model (DEM) and the Discrete Parcel Method (DPM). Both are based on tracking indi-

vidual particles or parcels of particles and finding local properties of the particles from the properties as the particles pass the point in the field.

The Discrete Element Method (DEM) tracks the motion and position (as well as other properties) of individual particles with time. The open circle in Figure 2.3a represents the one discrete element in the cloud. For each particle, fluid dynamic forces, contact forces and the moments due to neighboring particles are analyzed for the motion of the particle. Solving the equation of motion for all elements in the field gives the properties of the entire cloud. The method is suitable for unsteady and dense flows (e.g. particle-particle collisions). Examples of such applications are granular flows and fluidized beds [17].

The Discrete Parcel Method (DPM) follows a moving collection of particles, a so-called parcel (the open circles in Figure 2.3b). This parcel is treated as one *computational* particle with common dynamic properties. Further, the local properties of the cloud can be found when solved for the computational particle. DPM fits steady and dilute flows.

The coupling in multiphase flows generates numerous interphase forces, and the selected tracking of the particles needs to be introduced. In Langrangian particle tracking, each particle in the flow is treated separately. The equation of motion for each particle is defined by Newton's second law:

$$m_p \frac{d\boldsymbol{v}_i}{dt} = \sum \boldsymbol{F}_i, \tag{2.7}$$

where i refers to the i-th particle, m_p is the particle mass and $\mathbf{v}$ is the particle velocity. $\sum \mathbf{F}$ is all forces acting on the particle, but only the drag force is selected to act on the particles in this work.

Drag force is defined as:

$$F_D = \frac{1}{2}\rho_c C_D A(u-v)|u-v|, \tag{2.8}$$

where ρ_c is the continuous phase density, C_D is the drag coefficient, A is the reference area of the particle, and u and v are the fluid and particle velocities, respectively. C_D depends on particle shape and flow characteristics. C_D can be defined by the empirical correlation given by Schiller-Naumann [66]:

$$C_D = \begin{cases} \frac{24}{Re_r}(1 + 0.15Re_r^{0.687}) & Re_r \leqslant 1000 \\ 0.44 & Re_r > 1000 \end{cases} \tag{2.9}$$

The relative Reynolds number (Re_r) is defined by:

$$Re_r = \frac{\rho_c D|u-v|}{\mu_c}, \tag{2.10}$$

where ρ_c is the density of the continuous phase, D is the diameter (or characteristic length), μ_c is the viscosity of the continuous phase, and u and v are the fluid and particle velocities, respectively.

2.5.3 Turbulence

Turbulent flows are flows of random motion in space and time. Hinze et al. [28] defines it as "...an irregular condition of flow in which the various quantities show a random variation with time and space coordinates, so that statistically distinct average values can be discerned." Turbulence is characterized by chaotic movement in the form of cross-current and eddies.
Osborne Reynolds et al. [61] studied conditions when a flow changed from laminar to turbulent and found that the critical velocity was influenced by the following factors: the diameter of the tube, and the viscosity, density, and average linear velocity of the liquid. He grouped these factors into a dimensionless number, the Reynolds number as mentioned above.

Several observations have shown that the transition from laminar to turbulent flow covers a wide range of Reynolds numbers, but under ordinary conditions, a flow in a pipe or tube is turbulent at $\mathrm{Re} > 4000$, and the transition region goes from 2100 to 4000 [43].

There exist several computational approaches to turbulent flows, and they all fall under one of the two categories; **Simulations** or **Turbulence Models**. Turbulence modeling solves equations for mean quantities, while simulations solve equations for a time-dependent velocity field. In STAR-CCM+, the available turbulence modes are *Large eddy simulations*, *Detached Eddy simulation* and models that give closure to the Reynolds Average Navier-Stokes (RANS) equations. The latter is the method applied in this thesis, and it is based on decomposing the NS equations for the instantaneous velocity and pressure fields into a mean value and a fluctuating component. This results in an additional term in the momentum transport equations; the Reynolds stress tensor. To model this tensor in terms of mean flow values, a turbulent viscosity model named *k-omega turbulence model* is applied. The model solves two turbulence transport equations for turbulent kinetic energy k_t and the specific dissipation rate ω.

The k-ω model is a two-equation model. The k-omega model is known to work well near boundary layers under adverse pressure gradients, but most importantly it works well throughout the boundary layer. The model applied in STAR-CCM+ is the (Shear Stress Transport) SST (Menter) K-Omega model.

2.5.4 Wall Treatment

For each turbulence model, one assumes wall treatments (or functions), which are necessary to model near-wall regions, as turbulence models alone will not be able to precisely predict the flow in a turbulent boundary layer. Wall treatments are empirical equations which are used to satisfy the physics in the near-wall region. They are used to bridge the inner region between the wall and the turbulence fully developed region. When using the wall functions approach, there is no need to resolve the boundary layer causing a significant reduction of the mesh size and the computational domain.

Before further elaboration of this subject, we need to introduce some useful terms:

The dimensionless distance for wall-bounded flow, y^+ is defined as

$$y^+ \equiv \frac{u^* y}{\nu} \tag{2.11}$$

where

$$u^* = \sqrt{\frac{\tau_w}{\rho}} \tag{2.12}$$

In these equations y is the distance to the nearest wall, ν is the local kinematic viscosity of the fluid, u* is the reference velocity, τ_w is the wall shear stress, and ρ is the density.

We also need to introduce the dimensionless velocity, u^+, given by:

$$u^+ = \frac{u}{u^*} \tag{2.13}$$

where u is velocity.

The boundary layer region in need of modeling is the inner region, also known as the turbulent boundary layer. It can be be divided into three layers:

1. Viscous sub-layer (y^+ <5)
2. Buffer layer or blending region (5 <y^+ <30)
3. Fully turbulent or log-law region (y+ >30)

In the viscous sub-layer, it is assumed that velocity is linear and $y^+ = u^+$, while in the log-law region velocity it is logarithmic.

A mesh or grid needs to be created to achieve a precise prediction of the velocity gradient in the turbulent boundary layer. The first cell center needs to be placed in the log-law region for accurate results.

STAR-CCM+ offers three different wall treatments. This thesis uses the all-y^+ wall treatment for RANS. The all-y+ wall treatment is a hybrid treatment attempting to imitate the high-wall treatment for coarse meshes and the low-y+ wall treatment for fine meshes.

2.5.5 Particle Wall Collision and Erosion

When a particle collides with a wall, it rebounds but encounters a loss of kinetic energy due to friction and inelasticity effects. A restitution coefficient e is introduced to explain this energy loss, and it is given by the following definition:

$$e = \frac{v_Y^{(2)}}{v_Y^{(0)}}, \tag{2.14}$$

where $v_Y^{(2)}$ is the post-collisional velocity in y-direction, and $v_Y^{(0)}$ is the pre-collisional velocity in y-direction. If the value of e is one, it means that there is no mechanical energy

loss at the collision, and a value of zero would mean that it loses all mechanical energy, consequently being fastened to the surface.

Repeated particle-wall collisions may cause erosion, and CFD is a powerful tool in its prediction. There exist many different erosion models to apply in CFD, but the one selected for this thesis is the *Oka Model*, which is described in Chapter 3. Common for all models is their approach, which includes three steps: (1) obtaining a flow solution, (2) particle tracking and calculating the particle impact speed and angle, and (3) relating the particle impact information to mass loss of material through an erosion equation [88]. Each of these steps is dependent on the previous one, which sets high demands of accuracy to the first two steps. As particle impact information is given, it is saved for each CFD cell next to the wall. Further, the impact information is used to predict an erosion equation. Finally, the erosion equation from each particle is combined to an overall erosion equation for total mass loss.

Chapter 3

Literature Review

During the preparatory research for this study, a review of the published work regarding the erosion of nanofluid flows was done. This chapter covers relevant findings within erosion models, CFD modeling of erosion and experimental investigations of erosion by nanofluids.

3.1 Experimental Studies on Erosive Effects of Nanofluids

This section provides an overview of experimental work done on the erosive effects of impinging nanofluids onto various materials. Erosion by NF's has been found in several articles [9][10][58]. The presence of nanoparticles enhances the erosion rate (compared to the base fluid).

George et al. [24] studied the erosive effects of a 0.1 %-volume TiO_2/water (20-40 nm particle size) nanofluid on cast iron and aluminum. Tests were conducted at velocities of 5-10 m/s and impingement angles of 0° - 90°. Erosion was found to be at maximum close to 90° for cast iron, and 20° for aluminum, as shown in Figure 3.1. The material removal of cast iron was mainly due to corrosion-assisted erosion, while the aluminum smoothening was identified as a result of mild abrasive erosion. The maximum erosion rates observed for aluminum and cast iron targets were 2.5 mg/h and 1.5 mg/h, respectively. Some degree of work hardening was also observed for both materials.

Recent studies [9][10] investigated the effect of nanofluids impinging at flat metallic targets. The two studies examined aqueous nanofluids of TiO_2, Al_2O_3, ZrO_2 (each at 9% weight fractions) and SiC (at 3% weight fractions) onto aluminum, stainless steel, and copper targets. The NP sizes were reported as 20-30 nm (TiO_2), 100 nm (ZrO_2), 25 nm (SiC) and 100-200 nm (Al_2O_3). Tests were run with velocities of 5-6 m/s for 2-3 weeks. Estimations of the erosive effects were identified by using Scanning Electron Microscope (SEM) and an optical profilometer; measuring thickness reduction of the metallic targets. Firstly, stainless steel targets encountered negligible thickness reductions. Copper targets on the other hand did erode, and aluminum turned out to be the most sensitive material with significant mass losses (of about three hundred times the wear removal caused

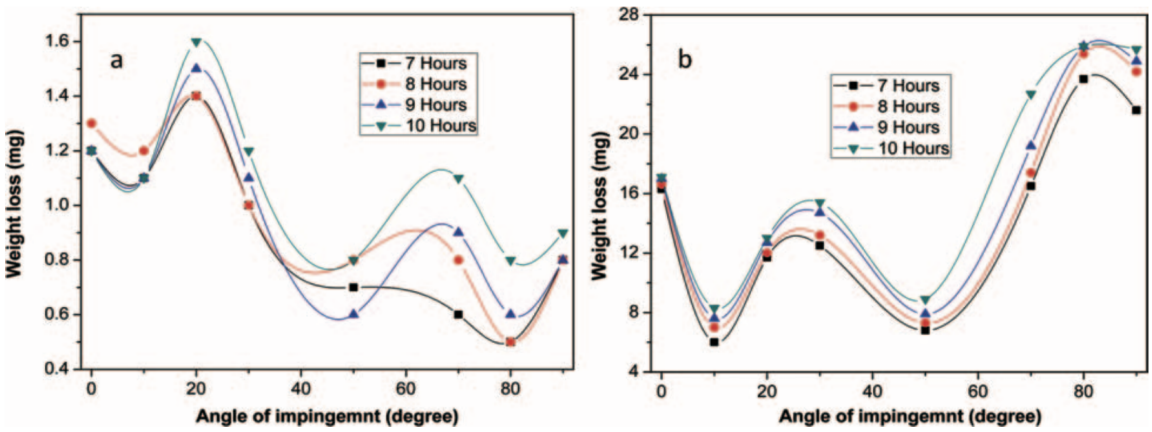

Figure 3.1: Weight loss of (a) Aluminum and (b) Cast iron during impingement of a 0.1 % TiO_2 nanofluid [24].

.

by water). Metals have previously been made known with their resistance to erosion being proportional to their hardness [59][76]. Aluminum has a lower hardness than copper (Vickers hardness around 170 MPa and 370, respectively). Additionally, aluminum is more chemically reactive than copper, which also explains its large mass loss.

The wear occurring to copper and mostly aluminum supports the theory of wear not being a result of the nature of the nanoparticles, but more of the target material and the pH of the fluid. Alterations in nanofluid concentrations also showed no change in the mass loss for both copper and aluminum targets. The hardness of the nanoparticle material was also found to be of negligible significance.

The particles shown to cause the largest wear were TiO_2, Al_2O_3 and ZrO_2. They are also the particles of the largest size: both for particle dimension and agglomerate dimension [9][10]. TiO_2 only caused erosion on aluminum targets, while SiC showed no erosive effects on any target material. The erosion mass fluxes of aluminum targets were 0.12 and $8.5{\cdot}10^{-4}$ g/h·m^2 for Al_2O_3 and TiO_2 (at 9% volume fractions), respectively [10].

Jet-impingement tests have found alumina/water nanofluids to erode both aluminum [9][44][46] and copper surfaces [9][44][45], but cause negligible erosive effects on stainless steel [9]. Additional tests found the flow of alumina/seawater nanofluids to cause mass loss of carbon steel due to the combined effect of erosion and corrosion [57][58]. The interesting finding of this study is the fact that alumina nanoparticles decrease the pure corrosion rate compared to seawater alone, but over time the inhibitory effect is lost and erosion-corrosion causes material loss. To sum up, the study found erosion-corrosion to cause more material loss than pure erosion and corrosion. Erosion-corrosion is an important aspect of erosion caused by NF's, as many NF's are based on metallic NP's.

Another study done on the erosive effects of alumina nanofluid (36 nm particle size) [46] concluded on potential premature damaging effects of the fluid. In further detail, an

aqueous nanofluid of 5% volume fraction was impinged at an aluminum surface at a velocity of $\approx$ 19 m/s. The 180-hour test resulted in a mass loss of 14 mg, where none of the mass loss was due to corrosion. This result corresponds to a mass loss rate of $7.778 \cdot 10^{-5}$ g/hr.

A study by Rashidi et al. [57] was able to isolate the effect of erosion alone and found erosive rates of alumina NFs (average particle of 20 nm) to increase by a factor of $\sim$ 10% compared to its base fluid, see Figure 3.2.

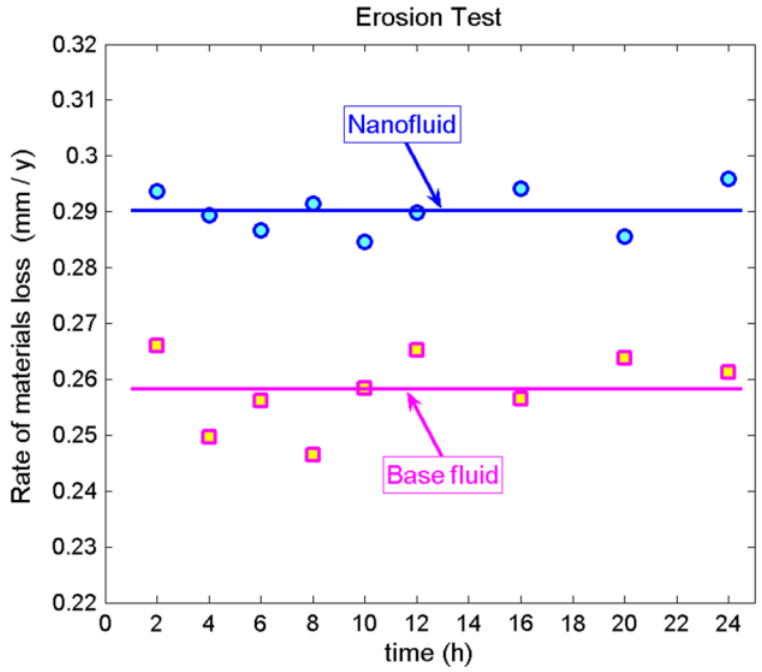

Figure 3.2: Nanofluid (Al_2O_3) and sea water (base fluid) erosion test results [57].

Another interesting finding is that of Bubbico et al. [9]; two concentrations of Al_2O_3 in water were shown to erode aluminum at very similar rates, even though one of the concentrations was three times the other concentration (3 and 9 wt%).

Several erosion studies have been performed using silicon carbide (SiC) NP's in water and cupric oxide (CuO) NP's in ethylene glycol. One study [63] performed tests of NF erosion in a car radiator. The volume fraction of SiC was 1-4 %, and of CuO 0.1-0.8 %, while impact velocities ranged from 4 m/s to 10 m/s. At impact angles ranging from 30° to 90° onto a Al3003 material surface, no erosion was found. The only wear found in one case (CuO/water NF at 90 and 9.6 m/s) was corrosion, causing a material loss rate at approximately 4 x 10^{-2} μm/hr. In a following study, Routbort et. al [62] investigated the possible erosion of an impeller made of Al3003. Cupric oxide and silicon carbide in ethylene glycol was used with 0.1-0.8 % (volume) and 0.5-4.0 % (volume), respectively. No erosion was found after more than 700 hours of impingement at 2% (volume) of SiC at 8 m/s.

Jiang et al. [33] investigated the compatibility of RAFM, 316L(N), and CuCrZr alloy with alumina-water NF's (10 nm particle size). The targets were exposed to NF with speed ranging from 1 m/s to 3.25 m/s for 1224 h and 2136 h. The CuCrZr alloy revealed severe wear compared to the two other materials. The experimental results indicate wear as a function of test duration, fluid velocity, and particle concentration.

Further experimental work is necessary to understand the erosion caused by NF's. To this date, the existing work covers different methods of identifying erosion. To be specific, most studies analyze the target material by using profilometers and SEM/TEM images. This provides information about the erosion pattern and magnitude. Few studies aim to find the quantitative wear, e.g. the mass loss and hence attain an erosion rate. Additionally, most present studies contain information about short-term erosive effects, but the possible applications of NF's require knowledge about long-term erosion.

Another comprehensive challenge to overcome is the study of erosive effects alone. Most heat transfer systems with the possibility of applying NF's are of metallic material. Many metals are highly sensitive to corrosion, hence most experimental erosion studies experience corrosion in addition to erosion. It is difficult to isolate the effect of erosion alone.

Finally, erosion is highly dependent on both target material and particle material. For this reason, there does not exist one generic model or relation for all nanofluids and system materials. There is a need to identify individual wear for each desired nanofluid and target material-combination.

3.2 Numerical Studies on Erosion due to Nanofluids

This section aims to elaborate on the available numerical erosion studies of relevance for erosion caused by nanofluids. There exist few numerical studies with nanometer-sized particles in multiphase flows, however significant amounts of similar studies with milli- or macrometer-sized particles. While the algorithm used in CFD for ordinary fluids would be similar when applied to nanofluids, it requires numerical adaption as the presence of NP's causes differences when solving conservation equations. NF modeling also arises challenges when selecting the correct approach; Eulerian-Eulerian or Eulerian-Langrangian.

Kamyar et al. [34] reviewed the aspect of implementing CFD for nanofluids. Firstly, it is of great importance to select correlations that attain valid properties for NF's to solve the conservation equations. NF's are also assumed to have low response times, resulting in both thermal equilibrium between the phases and a relative velocity of zero. Hence, one could apply the single-phase approach for modeling nanofluids [86], and many studies have reported reliable results applying this approach [1]. Yet it is important to note the existence of results contradicting this assumption [18]. A numerical study by Behzadmehr et al. [6] compared experimental results to numerical results for a Cu-water nanofluid in a tube. Both the single-phase and two-phase approach were implemented, finding the two-phase approach to agree better with the experimental values. It is to be noted that the studies recommending the two-phase approach model heat transfer, and future work is necessary to identify the best approach for different applications.

As for erosion modeling with nanofluids, the few existing ones are summarized here. A numerical study conducted by Kosinska et al. [36] investigated the erosive effects of micro- and nanosized particles (10^{-8} to 10^{-3} m) in pipe elbows. As expected, increasing fluid velocity and particle diameter promoted erosion rate. However, for particles smaller than 100 μm the maximum erosion rates reached the highest levels for smaller particles. This was explained by the formation of secondary flows pulling the smaller particles towards the elbow wall. Nevertheless, this observation did not occur to nanoparticles, as their low mass does not cause enough damage to erode the wall. A critical diameter of $1.0{\cdot}10^{-5}$ m was observed which below erosion rate increased until a second critical point was reached and erosion rate decreased again. Additionally, this phenomenon was observed with largest rate for the lowest applied velocities (lower than 2.0 m/s).

A paper by Safaei et al. [64] treated copper-water nanofluid as a two-phase mixture when numerically predicting erosion in 90° elbows. Copper particles of diameters from 10 nm to 100 microns were simulated with velocities ranging from 5-20 m/s through an elbow. Volume fraction was selected to range from 0%-4%. Using the DPM model, the results shows maximum erosion rate, average erosion rate, and total erosion rate to increase with particle diameter, volume fraction, and fluid velocity. For instance, the total erosion rate is found to increase with a factor of 8 when the volume fraction is increased from 2% to 4%. Additionally, a threshold velocity as well as a threshold particle size can be identified, beyond which erosion is significant.

Erosion in pipe bends by micro- and nanoparticles (10^{-6} m and 10^{-9} m particle diameter) has also been numerically investigated by Shinde et al. [69]. The erosion rate was found to be determined by particle impact angle and turbulence secondary flow. The micro particles showed higher erosion compared to nanoparticles for nearly every operational condition. However, at bend angles higher than 100° and identical radius of curvate, the erosion was nearly identical for micro- and nanoparticles.

Gnanavelu et al. [25] developed a prediction model to specify wear profiles for a 2-D jet impingement test of water and sand (250 μm particle size). The model was obtained from material wear data from experiments and CFD simulations. A good correlation was found between the predicted and experimental data. Nonetheless, errors are inherent in the model due to assumptions regarding particle shape and size, material hardening, and numerical approximations.

Wang et al. [81] also studied slurry erosion, by both collecting experimental data and by CFD simulation. By using a sand/water (200 μm particle size) mixture, erosion was studied as a result of impingement velocity and sand concentration. Additionally, tests were run both with specimen submerged in the fluid or being above the fluid level. Submerging the specimen resulted in a "W" scar shape. The predicted data were found to agree with the weight loss measurements.

Mansouri et al. [42] performed a combined experimental and numerical study to study the erosion pattern of a submerged impingement. Both gas-solid and liquid-solid flows were performed, and results found solid particles (300 μm particle size) to follow the liquid stream by far more than for gas-solid flows. For the numerical investigation, the Eulerian-

Langrian approach was selected, in addition to DPM for particle tracking. The rates found by experiments showed similar erosion rates to the ones predicted by CFD. While experimental results deviated a small amount from numerical results for an impingement angle of $\theta = 45$, a closer result was found when the impingement angle was selected as $\theta = 90$. Liquid testing and numerical analysis show an erosion pattern shaped like a W, which supports the findings of Wang et al. [81]. Both Mansouri et al. [42] and Wang et al. [81] attained a 10-20% difference between experimental and predicted erosion rates.

3.3 Erosion Models

Multiple models have been developed trying to relate parameters to erosion rate. Today there exist over 200 reported erosion models [30]. Despite the large number of models existing, no model is yet to precisely forecast the erosion rate only given impact parameters and material properties.

In general, one can can express erosion as a function of the following:

$$\text{Erosion} = f(\text{operating conditions, properties of the particles, properties of the target material})$$

There exist both numerical and analytical models proposing the rate of erosion in various geometries. While analytical often are more precise, numerical models have the benefit of being less costly and time-consuming. The CFD software STAR-CCM+ has five available erosion models; Ahlert, DNV [79], Neilson-Gilchrist, Oka [50] and Archard. The Oka model is the one chosen for erosion modeling in this thesis.

The Oka model is an empirical correlation as it takes into account target material hardness and particle diameter. The authors modified classic/established equations by including a previously neglected factor, namely the hardness of the surface material. This factor is a characteristic of solid material, expressing its resistance to permanent deformation. Consequently, the Oka model is a more realistic correlation than previously established models. The Oka model is built on the idea that erosion wear is the product of two factors, where the first factor is related to the vertical component of the impact energy and approximates repeated plastic deformation, while the second factor indicates the approximately horizontal component related to the cutting action.

The model is given by the following relations:

$$ER = g(\theta)E_{90} \tag{3.1}$$

$$g(\theta) = \sin(\theta)^{n_1}(1 + Hv(1 - \sin(\theta))^{n_2} \tag{3.2}$$

$$E_{90} = K(Hv)^{k_1}\left(\frac{V_p}{V'}\right)^{k_2}\left(\frac{D_p}{D'}\right)^{k_3} \tag{3.3}$$

where ER is the volumetric erosion damage [mm^3/kg] at an impact angle θ, E_{90} is the erosion damage at normal impact angle, Hv is the Vickers number in GPa; measuring the wall material hardness, V_p and V' [m/s] are the particle impact speed and the user-specified reference speed, respectively; D_p and D' [μm] are the particle diameter and the user-specified reference diameter, respectively.

The exponent factors k_1, k_2, and k_3 are determined by properties of the particle, with material hardness also determining k_2. K is an independent factor denoting particle properties such as particle shape and particle hardness. The exponents n_1 and n_2 are determined by material hardness and other impact conditions such as particle shape.

When used in STAR-CCM+, the model applies a user-specified reference speed and diameter of 104 m/s and 326 μm, respectively.

Although the Oka model was an updated erosion correlation at its release date, it does encounter some limitations. First, the sharpness of impacting particles is not accounted for, and the model was developed for particles moving in air flow at high velocities (50 m/s), limiting its validation for incompressible fluids. Such high velocities are seldom found in industrial applications such as oil and gas. Additionally, the empirical constants of the model are based on specific experimental conditions not necessarily applicable to other circumstances. Obtaining the constants for a specific erosion problem might also encounter challenges. Yet, Oka et al. state that the equation "can be utilized under any impact conditions and for any type of material".

To summarize, there exist large amounts of papers on the subject of nanofluids, although their erosive effects need to be further investigated. Both numerical and experimental studies agree on factors enhancing erosion rate; such as impact velocity, particle size, and particle concentration, which in total contributes to the impact energy. Yet, experimental studies indicate corrosion as a larger wear impact than pure erosion for metallic materials submerged in the operating fluid. Hence, the combined effect of corrosion and erosion for nanofluids in recirculating systems needs further analysis. Additionally, erosion rates of various sizes are found based on the specific combination of nanofluid and target material, implying the need for an investigation of the distinct nanofluid before applying it to a system.

Chapter 4

Methodology

This chapter contains a description of the conducted experiments and their preparation. Additionally, it describes the numerical model used for erosion prediction in this thesis.

4.1 Experimental Details

4.1.1 Materials

Titanium dioxide powder (>99.5%) was purchased from Sigma-Aldrich (see Figure 4.1). PVP (polyvinylpyrrolidone) was used as surfactant. PVP is a non-toxic and non-ionic water-soluble polymer surfactant [35]. Distilled water was used as base fluid.

Figure 4.1: TiO_2 Nanoparticles

The selected NP's are traditionally used as pigments in cosmetics and printing but have been given attention in NF research due to their stability and non-toxicity. Figure 4.2

shows a SEM-image with 10^5 magnification of dry TiO_2 nanoparticles. Relevant properties of the TiO_2 particles are given in Table 4.1.

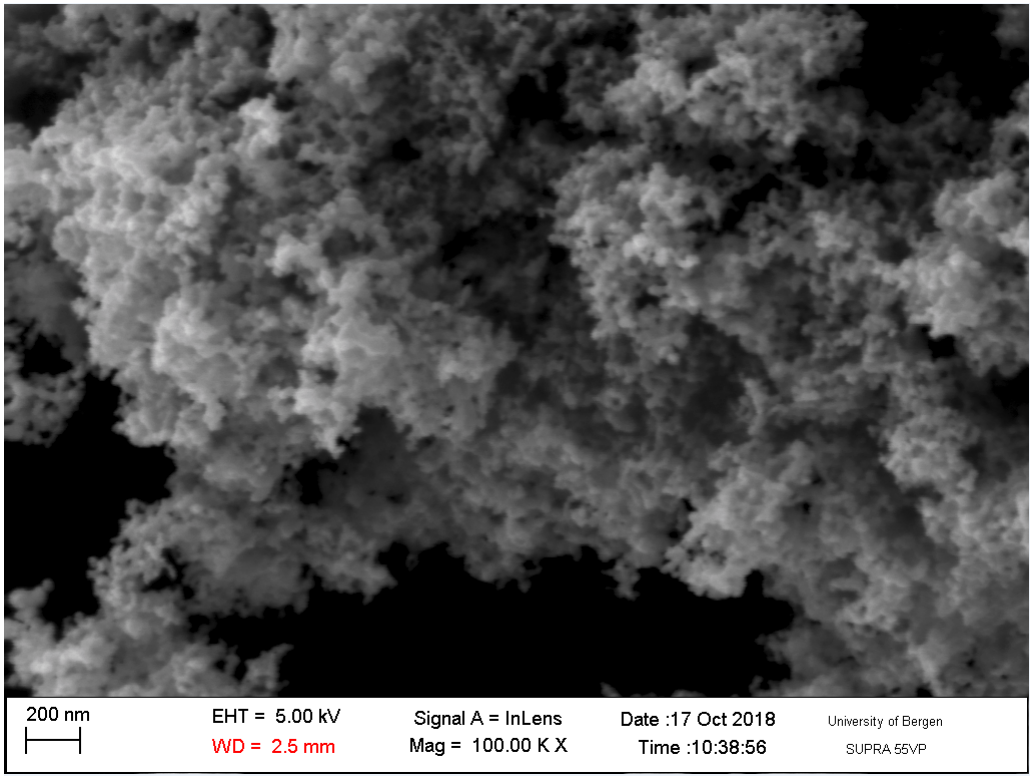

Figure 4.2: SEM image of TiO_2 nanoparticles

Table 4.1: Properties of TiO_2

Property	Value
Density	4260 kg/m^3
Primary particle size	21 nm
Vickers hardness	1121 kg/mm^2 [9]
Molar Mass	79.87 g/mol

4.1.2 TiO_2 Nanofluid Preparation and Characterization

The preparation of the TiO_2 nanofluid was done by using the two-step method mentioned in Section 2.2. TiO_2, PVP, and distilled water were weighed separately by the use of an analytical scale, namely Kern 440-33N. Further, nanoparticles were dispersed in the distilled water, continued by the addition of the surfactant. The components were roughly mixed before being properly dispersed using an ultrasonic bath for two hours. A Brandson 3510 ultrasonic cleaner was used. Finally, the finished nanofluid was visually examined for full dispersion. The nanofluid showed good stability. It should be noted that the nanofluid reached a temperature of $\sim$50°C during sonication.

A total amount of 16 L of nanofluid was needed for the erosion set-up. Due to a lack of large containers, nanofluid was produced 1 L at a time, for further mixing in a 5 L container. To ensure proper dispersion, the 5 L containers were sonicated for 1 hour before added to the set-up.

The selected concentration of the nanofluid is 6% weight fraction (wt.). Distilled water was chosen as base fluid as it is inexpensive. Further, PVP was chosen as a surfactant as it showed better stability than other surfactants available in the laboratory, in addition to its high solubility in water. The weight ratio of nanoparticles and surfactant was chosen as 1:1.

4.1.2.1 Particle Size Distribution

The fluids used for the experiments were analyzed to find their particle size distribution (PSD) using static light scattering (SLS).

The technique of SLS is based on the absorption and scattering of light caused by a particle interacting with light. The light scattered by one particle has an absolute intensity q, from where the average size of a particle is obtained. This relationship is described by the Rayleigh theory, which states larger particles to scatter more light than smaller particles exposed to a given light source. In other words, the intensity of the scattered light is proportional to the particle molecular weight and size [75].

SLS experiments are done by using a high-intensity monochromatic laser on a sample containing the investigated particles. One or more detectors are used to quantify the intensity's dependence on the scattering angle ϕ. Measurements at multiple angles provide a scattering curve of intensity as a function of ϕ, which gives accurate values of both molecular weight and particle size for all scattering particles. SLS is also often used to obtain the size of particle suspension in sub-µm and supra-µm ranges.

The SLS instruments used for this work are the Malvern Mastersizer 2000 and the Analysette Nanotec Fritsch 22 laser. Nanofluid samples were dispersed in filtered tap water and kept in suspension by a mechanical stirrer. The speed of the mechanical stirrer and the pumping power were controlled at low levels to avoid bubble formation. The Malvern Mastersizer uses an internal sonication probe operating with a power of 70W and a frequency of 22 kHz, according to the manufacturer.

The results from the SLS experiments are given as volume frequencies. The number density can be obtained from the given data. The size distributions of nanoparticles are often normally distributed and can be presented by the following function:

$$f_n(D) = \lim_{\Delta D \to 0} \frac{\tilde{f}_n(D)}{\Delta D}, \tag{4.1}$$

where $\tilde{f}_n$(D) is the frequency of particles with diameter D. In terms of volume frequency, $\tilde{f}_n$(D) is the volume fraction of particles with diameter D $\in [D, dD + D]$

The Malvern Mastersizer is based on volume frequency, which can give a failing image of the represented particles. To illustrate, the intensity of a particle with 100 nm diameter is 10 times bigger than a particle with 10 nm diameter. As 10 particles of 100 nm diameter make up a larger volume than 100 particles of 10 nm, the larger particles will dominate the size distribution. In number frequency-based PSD on the other hand, the intensity is simply the number of particles corresponding to a specific diameter. It is therefore often beneficial to convert volume frequency to number frequency for particles of small diameters.

4.1.3 Erosion Setup and Test Specimens

The experimental setup for erosion testing was developed at the Western Norway University of Applied Sciences and is shown in Figure 4.3a.

(a) The erosion setup.

(b) The sample holder inside tank.

Figure 4.3: Experimental setup at HVL.

Table 4.2: System description

Component no	Description
1	Aluminium tank
2	Sample Holder
3	Valve
4	Pump
5	Valve
6	Flow Meter

Figure 4.4 provides a more detailed illustration of the set-up, with main components listed in Table 4.2.

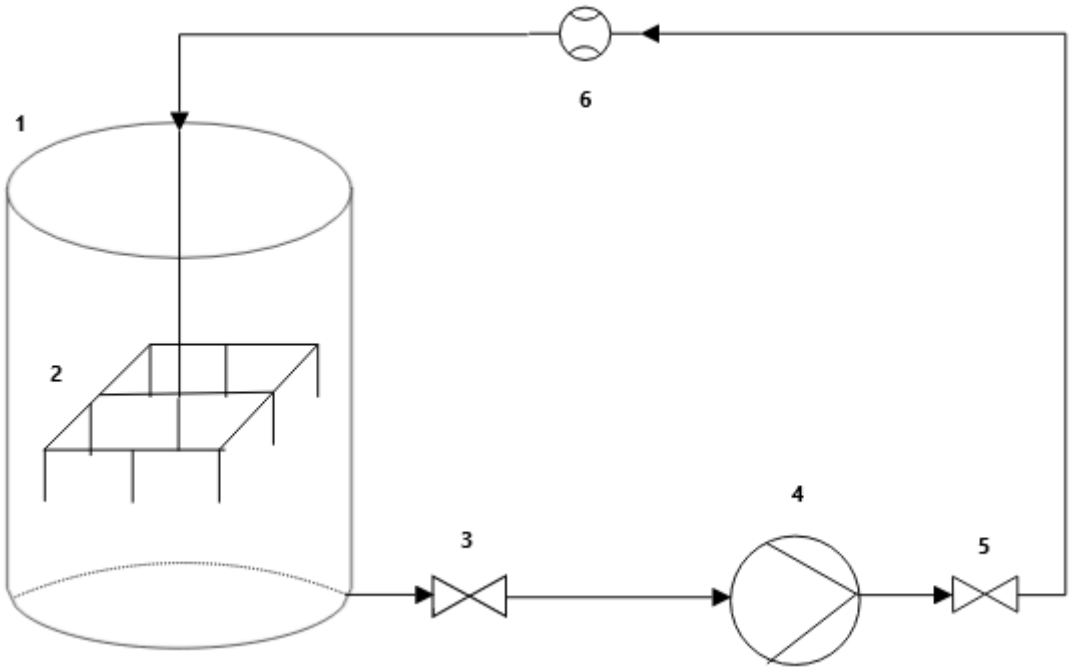

Figure 4.4: Schematic figure of the erosion system.

The experimental system consists of a closed liquid circuit with a pump (4), a flow meter (6), and a large tank (1) enclosing the material sample holder, as shown in Figure 4.3a. The rig is manufactured to expose nine material targets to a low-speed simultaneous 90° impingement, as shown in Figure 4.3b. There are a total of nine nozzle outlets, which all have a distance to the material targets of 8 mm. The pump selected is a Nocchi VLR 8 - 30 A; a vertical multi-cell centrifugal pump.

The sample holder consists of a square metal grate connected to a metal post on each side. Nine metal rings are glued to the upper surface of the grate, to keep the material targets in place. As shown in Figure 4.3b, there are three targets for each material. The materials chosen for this work are copper, plastic (PVC), and rubber (natural rubber). Each target is cut into circular plates of 2 mm thickness and 29 mm diameter, as shown in Figure 4.5. The specific target materials were selected to investigate other materials than metals alone. Most experimental work done in literature to this point has investigated metals such as aluminum, stainless steel, and copper. Copper was selected as it is often used in heat transfer systems, but also as the resulting erosion rate can be compared to rates found in previous works. Additionally, rubber and PVC was selected as they are softer materials, so that one might observe a larger erosion rate than for copper. Rubber and various plastic types are found in smaller components of heat transfer systems.

Figure 4.5: Material samples: rubber, copper and plastic

A thermometer was placed outside the tank with a wire inside the tank and submerged in the fluid so that one could record the liquid temperature. The initial temperature of the fluid was $\sim$ 20°C. The continuous flow recirculation causes a temperature rise and consequently evaporation of the fluid. The mean temperature of the fluid during the test was 61.2°C. To prevent a reduction in fluid volume, a lid was constructed and placed over the tank. The evaporated base fluid was condensed at the lid and recycled to the system under the gravity. Additionally, studies indicate the presence of nanoparticles in the condensate of boiled nanofluids [78], which can cause alteration in the NF concentration.

The system consists of a tank of 44.5 cm inner diameter connected to rubber tubes. The upper inlet of the sample holder is a copper tube of inner diameter 1.62 cm. The copper tube separates into nine identical nozzles configured in a grid. Each nozzle is of 3 mm inner diameter and 5.52 cm length.

As this study aims to find an erosive rate of nanofluid, most conditions are chosen with as high values as possible. Hence, a stable NF of high concentration was chosen to have as many eroding particles present in the fluid as possible. Additionally, one can regulate the flow of the system by the use of the nozzle placed at the pump outlet, but it was chosen to be fully open at all times. This allows the time rate of particles impinging the targets to be at maximum (considering the chosen system). It is also to be noted that the flow rate of the system was only read by a flow meter, and not controlled in a way to keep flow rate constant.

4.1.4 Experimental Procedure

Experiments with the erosion rig were conducted as shown in the following.

At first, a total of 20 L tap water was added to the tank (containing the target specimens). The system was left running for approximately a month. This was done to investigate any possible problems with the erosion rig, as well as the possible erosive effects of water alone. After shutting down the system, the target specimens were dried and studied using SEM, and the results are shown in section 5.3. Additionally, the targets were weighed for identifying mass losses caused by erosion due to natural contamination of the rig by the airborne particles.

A second test with water as operational fluid was conducted. The main problem encountered after finalizing the test with tap water was the generation of a corrosive coating. The corroded material was mostly clusters of particles strongly adhered to the inner surface of the tank. Clusters were also found inside the pipe in- and outlets. The tank was thoroughly cleaned to remove most of the corrosion. As this study aims to investigate erosion alone, an effort was made to prevent further corrosion for experiments with nanofluid as the operating fluid. The parts of the sample holder made of aluminum were coated with Bengalack to reduce contact between the operating fluid and the corroded surfaces. Additionally, a large plastic bag was put as a layer between the tank wall and the sample holder, to decrease the contact surface between the fluid and the tank walls. Also, a hole was made by the outlet of the tank.

After this, the production of large amounts of nanofluid was carried out. A total of 16 L of 6 wt.% TiO_2 nanofluid was produced. Followingly, the water contained in the erosion rig was removed from the erosion rig, and replaced with the total amount of nanofluid. Nevertheless, the system encountered problems when operating with nanofluid and the pump shut down after running for approximately two minutes.

The nanofluid was then emptied from the system, to identify the cause of the problem. Possible issues were investigated, such as clogging of the system due to the plastic bag or other materials. The problem was not identified, but it was assumed to be the increased viscosity of the nanofluid compared to that of water. Having replaced the pump, the system was able to run undisturbed.

At the start of the third test, a total of around 35 L of water was added to the tank. To avoid the problems of the previous run, a decision was made to add small amounts of nanofluid at a time. This way one was able to control how the pump "reacted" to changes in viscosity. A total of 5 L of nanofluid was added after 48 hours.

An additional 5 L of nanofluid was added to the system after 96 hours. The resulting nanofluid has a significantly lower concentration than the originally manufactured nanofluid. Thus, the components of the operating fluid were ∼35 L of tap water and 10 L of 6 wt.% TiO_2 nanofluid. Hence, the new concentration W_m for the TiO_2 nanofluid becomes:

$$W_m = \frac{600g}{45000g} \approx 0.0133 = 1.33wt.\%$$

A sample of the operating fluid was withdrawn after 96 hours. The sample was analyzed using the Malvern Mastersizer 2000 to obtain information about possible agglomeration or sedimentation of the nanoparticles. The original goal was to regularly withdraw samples from the tank to study the changing size distribution with respect to time. Due to the shortened test duration, only two samples were collected: at the start and the termination of the test. The fluid samples have been analyzed and the results are presented in Chapter 5.

The test was terminated after a total test duration of 334 hours. After test completion, the material specimens were analyzed by weighing to provide the quantitative erosion rate. Post-test images were also taken by the use of SEM imaging. These images are presented in Chapter 5.

4.1.4.1 Flow Meter

The selected flow meter measured the amount of nanofluid flowing through the pipe for the NF test (with the newest pump). The flow rate was read off regularly after start-up. The flow rate started at 0.1905 m^3/h, with a small, constant increase. The detected flow rates are shown in Figure 4.6.

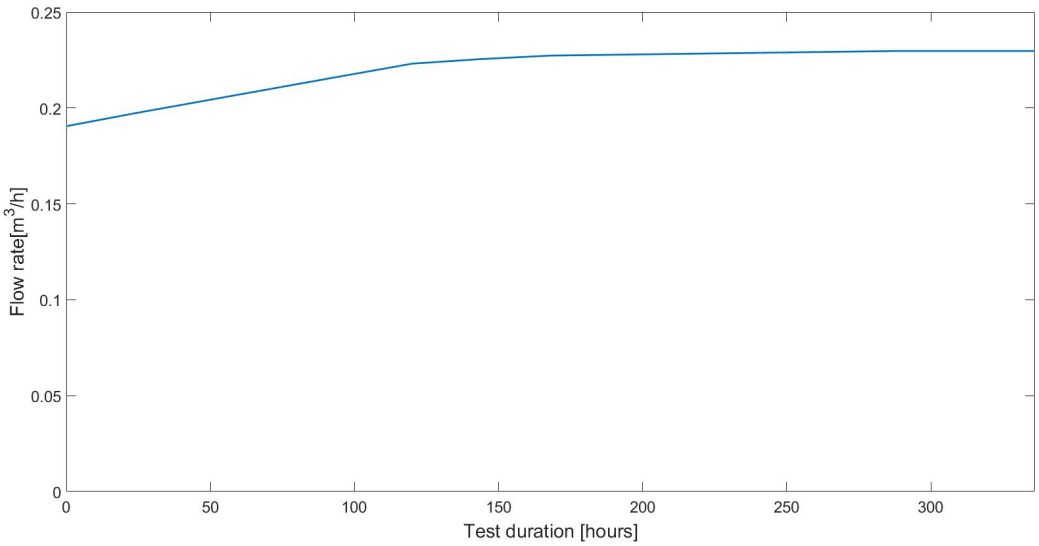

Figure 4.6: Flow rate during NF erosion test

The three final flow rates were observed as 0.2297 m^3/h. However, the flow meter had stopped its detection at those readings. Hence, the flow rates were most likely higher than the observed value. The same problem occurred during the test with water as operational fluid.

The detected enhancement of flow rate can be explained by numerous factors. Primarily, the sedimentation of NP's is believed to increase with time, which resulted in a lower

viscosity. This effect is accounted for by the pump, hence resulting in an enhanced flow rate. The changes in cross-section area throughout the system cause a pressure drop causing a higher pumping power. It is also to be noted that the flow meter fluctuates and has an instrumental uncertainty.

Nonetheless, one can find an approximate value of the total volume exposing the targets through the test duration, by selecting a trend line for the graph. As the final values were most likely of higher value than the flow meter showed, one can assume the values to follow linear regression: Flow rate, $\dot{Q}$ for a given hour, h after start can be linearly approximated to:

$$Q(h) = 0.0001h + 0.2019 \tag{4.2}$$

To find the total volume exposing the targets for the test run, the relation was integrated from start to end:

$$\int_0^{336} (0.0001h + 0.2019)dh$$

$= 73.4832$ m^3 $\approx$ 73 480 L

The observed flowrates can be further treated to estimate the outlet velocity for each nozzle. The outlet velocity can be found by using the continuity equation in addition to assuming the NF as incompressible. Note that the fluid stream splits into nine nozzles. When implementing the continuity equation, the initial and final observed flowrates corresponds to outlet velocities of 0.83 m/s and 1.0 m/s, respectively. These values will be further applied in the numerical investigation.

4.2 Methodology for Simulation of Nanofluid Erosion

This section describes the numerical set-up for the simulations done in STAR-CCM+. By selecting the appropriate models, one can predict the local erosion rate in the specific geometry.

The modeling is done to investigate the influence of the following parameters on erosion:

- effect of particle size
- effect of injection velocity
- effect of particle material density

4.2.1 Geometry and Mesh

The developed geometry represents one of the nine nozzles in the experimental set-up. Below the nozzle outlet is the target specimen. The nozzle outlet has an inner diameter of 3 mm, and there is a distance of 1.7 cm between the outlet and the surface of the target. The flow out of the nozzle is vertical downwards, and impinges at a target of a 3 cm diameter.

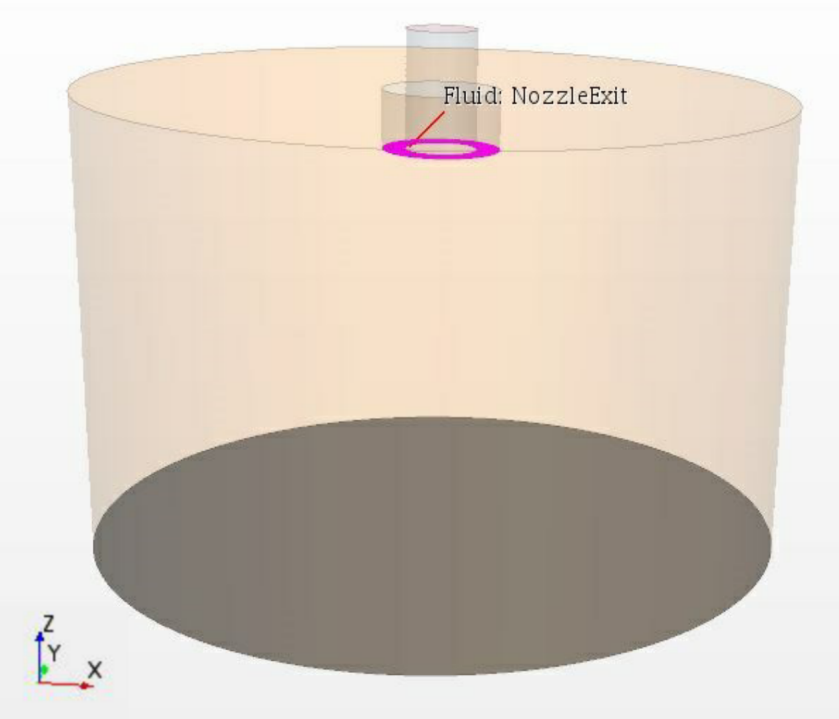

Figure 4.7: Illustration of the nozzle outlet, where the particles are subjected

Figure 4.8a shows the mesh chosen for the simulation. The three-dimensional cells are ordered in the geometry and result in a closed volume. These cells are developed for solvers using the finite volume method. The core meshers were selected as polyhedral mesher and

prism layer mesher. Also, surface remesher was selected. The number of prism layers was selected as two, with a total thickness with an absolute size of $1.3332 \cdot 10^{-4}$ m.

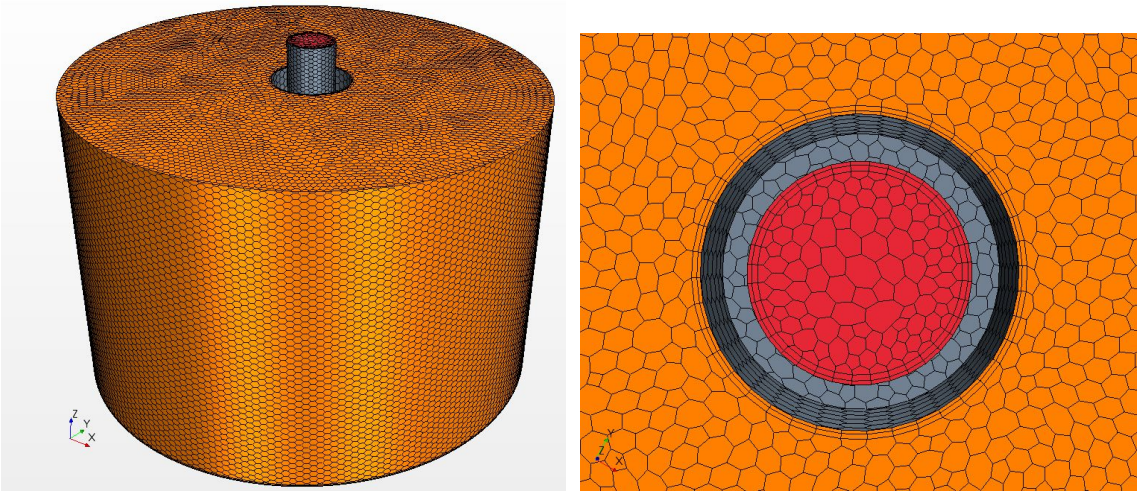

(a) The selected mesh.

(b) The mesh around the nozzle inlet.

Figure 4.8: The mesh chosen for simulations. Base size is set as $4.0 \cdot 10^{-4}$m.

4.2.2 Models and Solvers

This section describes all the models defined for this work in STAR-CCM+. A model defines how a physical phenomenon in a continuum is represented, and their major purpose is to work with solvers to obtain a solution. All models and solvers selected for this work are used for every performed simulation. The selected time step is 0.001 s.

The models and their chosen solvers for the continuous and dispersed phase can be found in Tables 4.3 and 4.4, respectively.

Table 4.3: Models and solvers used for continuous phase modeling

Common models	**Solvers**
All y+ Wall Treatment	
Constant Density	
Exact Wall Distance	Implicit Unsteady
Implicit Unsteady	Partitioning
K-Omega Turbulence	Wall Distance
Langrangian Multiphase	Langrangian Multiphase
Liquid	Segregated Flow
Reynolds-Averaged Navier-Stokes	K-Omega Turbulence
Segregated Flow	K-Omega Turbulent Viscosity
SST (Menter) K-Omega	
Three Dimensional	
Turbulent	

Table 4.4: Models and solvers used for dispersed phase modeling

Common models	**Solvers**
Constant Density	
Drag Force	Implicit Unsteady
Erosion	Partitioning
Material Particles	Wall Distance
Pressure Gradient Force	Langrangian Multiphase
Solid	Segregated Flow
Spherical Particles	K-Omega Turbulence

4.2.3 Boundary and Initial conditions

In this section, the boundary and initial conditions applied for the simulations are described. Boundary conditions are the conditions at the surfaces surrounding and defining a region, while the initial conditions are the starting values of the simulation. Initial conditions are given for the continuous phase in Table 4.5, and the boundary conditions are given in Table 4.6.

Table 4.5: The initial conditions for the continuous phase

Parameter	Initial Value	Unit
Pressure	0.0	Pa
Turbulence Intensity	0.01	-
Turbulence Specification	Intensity + Viscosity Ratio	-
Turbulent Velocity Scale	1	m/s
Turbulent Viscosity Ratio	10	-
Velocity	[0.0, 0.0, 0.0]	m/s

Table 4.6: The boundary conditions for the continuous phase

Boundary	**Boundary Condition**
Inlet	Inlet Velocity
Nozzle Exit	No-slip wall
Nozzle Inner Wall	No-slip Wall
Sample	No-slip Wall
Upper Side	Pressure Outlet
Sides	Pressure Outlet

There are also *Reference Values* for the physics continuum, shown in Table 4.7.

Table 4.7: Reference values for the continuous phase

Parameter	**Reference Value**	**Unit**
Reference Pressure	101 325	Pa
Minimum Allowable Wall Distance	$1.0 \cdot 10^{-6}$	m

Finally, it is also to be noted that the target material can not be selected for erosion modeling in STAR-CCM+.

4.2.4 Particle Injector

For the simulations in this work, particles are defined in the Langrangian phase. The particles enter the computational domain through injectors at one or more discrete locations. The injectors define the direction and frequency of particle flow into the domain. The inlet velocity for the particle injector is selected as it is in the same range as the value in the experimental erosion test.

The injector for this work is selected as *Part Injector*. A part injector represents a selection of injection points derived from the geometry of the injector [71]. Figure 4.9 illustrates the system with particles injected from the inlet.

The settings for the particle injector are found in Table 4.8.

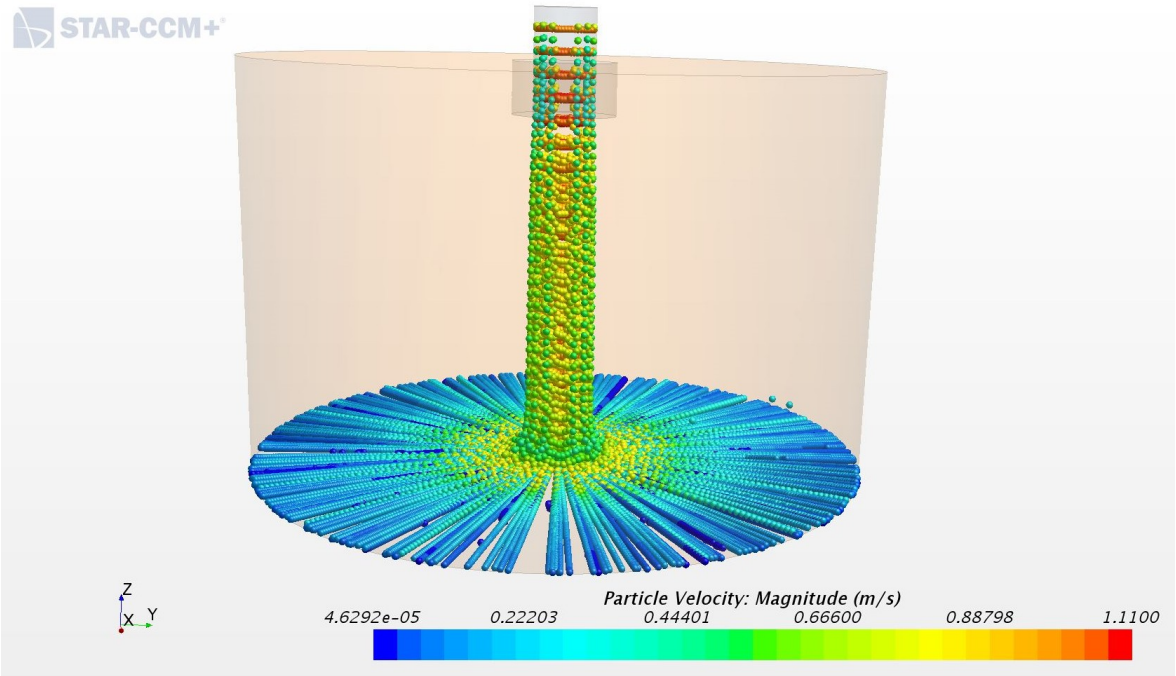

Figure 4.9: Particle flow from the injector

Table 4.8: Settings for the particle injector

Conditions		
Flow Rate Distribution	Per Injector	
Flow Rate Specification	Mass Flow Rate	
Particle Size Specification	Particle Size	
Time Randomization	-	
Velocity Specification	Components	
Values		
Parcel Streams	1.0	-
Point Inclusion Probability	1.0	-
Mass Flow Rate	1.0	kg/s
Particle Diameter	-	m
Inlet Velocity	[0.0, 0.0, -1.0]	m/s

4.2.5 Particle Flow and Simulation Procedure

The particle flow parameters are the ones being altered for the various scenarios this work aims to investigate.

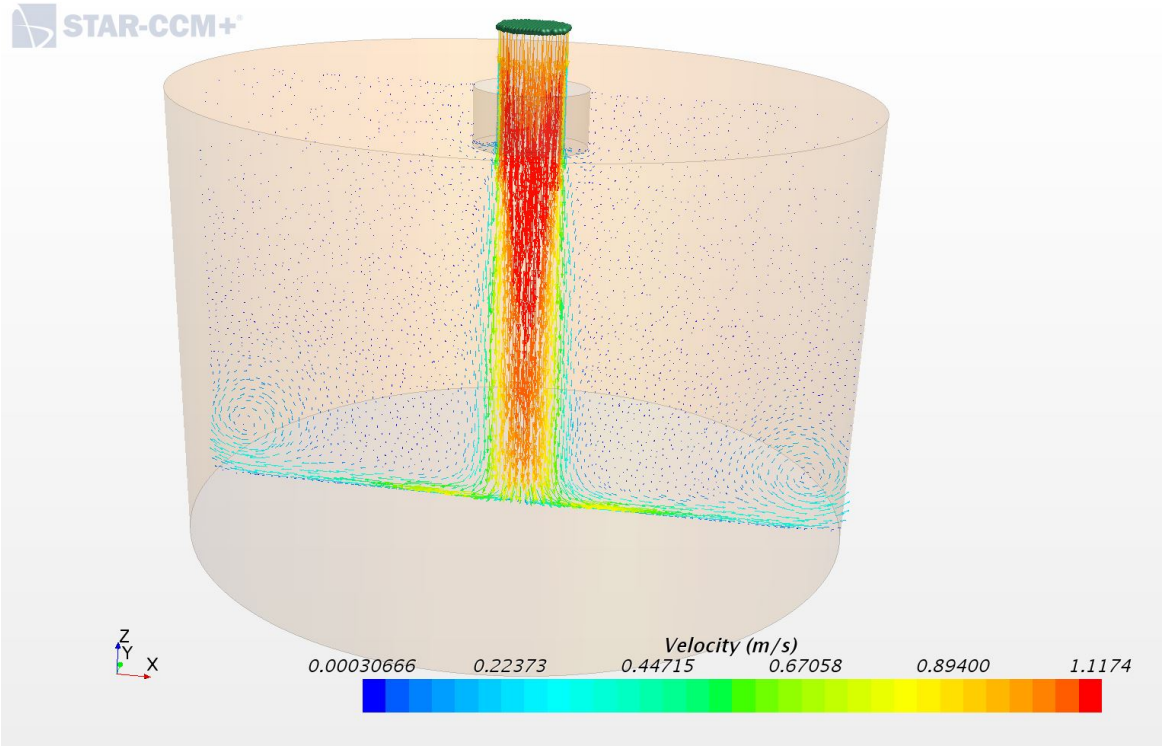

Figure 4.10: Cross-section of the fluid velocity

Table 4.9: Description of the range of process parameters used in the simulations

Process parameters	**Value**	**Unit**
Particle size, d_p	$\in [1.0{\cdot}10^{-6}, 1.0{\cdot}10^{-3}]$	m
Density, ρ_d	$\in$ [1000, 10 000]	kg/m^3
Drag force, F_D	Schiller-Naumann	-
Inlet velocity, V_0	$\in$ [-1.0, 0.0]	m/s

Chapter 5

Results and Discussion

5.1 Experimental Investigation

5.1.1 SLS Analysis

During the final erosion tests, a combination of tap water and NF was used as the running fluid. As mentioned in Chapter 4, pure NF was not used for the final erosion test due to previous problems with the operating pump. Hence, tap water alone ran in the system at first. Thereafter, small amounts of 6 wt.% NF was added regularly until the total fluid volume included 10 L NF, resulting in a final NF concentration of ∼1.33 wt.%.

Various fluids were involved with the erosion tests. Samples were collected from the following fluids for further SLS analysis:

- 1 L of 6 wt.% NF
- 5 L of 6 wt.% NF (Note that 1 L was made at the time, with five samples being mixed in a tank. This is before addition to the erosion set-up.)
- Tap water sample from erosion set-up
- Sample from erosion set-up containing 10 L NF (before erosion test)
- Sample from erosion set-up containing 10 L NF (after erosion test)

The SLS analysis aims to investigate the effect of test duration and merging of NF samples concerning fluid stability and agglomeration. As described in Chapter 4, number frequency is often a better representation for PSD when analyzing smaller particles. Thus, this chapter only contains normalized number frequency PSD plots.

Figure 5.1 shows the PSD of the two NF samples. The size distribution of the NP's is shown to range from 0-400 nm and 0.5-2 μm for the 1 L sample and the 5 L sample, respectively. When comparing the two samples, one can observe high stability for the 1 L sample, as its shift shows a peak at $\sim$ 40 nm, which twice the particle size given by the manufacturer (Sigma-Aldrich, 21 nm). The 5 L sample on the other hand yields a shift

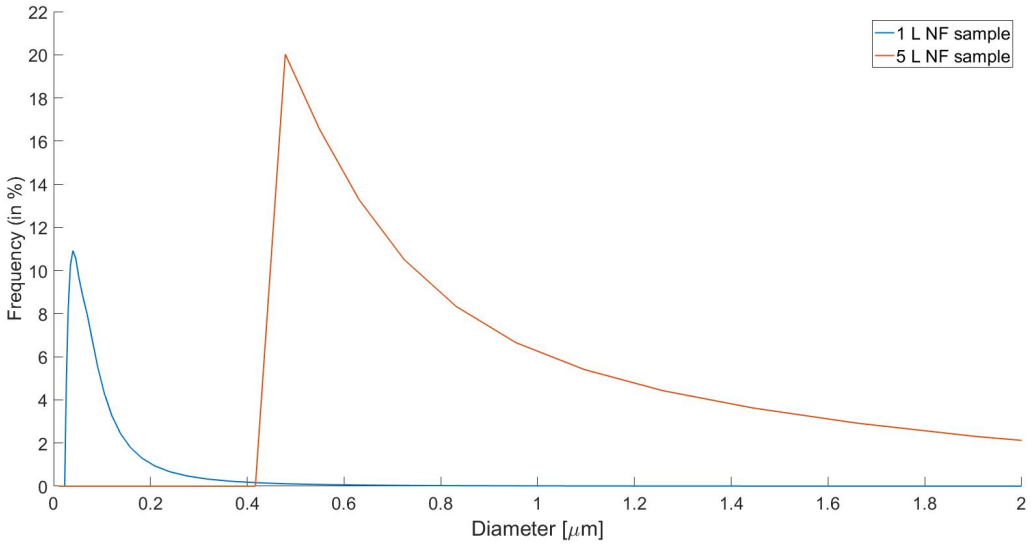

Figure 5.1: Normalized number frequency of original NF compared to a 5 L merged NF sample.

further to the right, with particles ranging from 500 nm to 2μm. Subsequently, merging NF samples reduces stability and causes agglomeration. Regardless of the agglomerates, particle size is relatively small for both samples, but the categorization of the 5 L sample as a NF is questionable.

As for the tap water, it was added to and run in the set-up for 48 hours before withdrawing a sample. As a result, it became sludgy, which is most likely a result of particles of aluminum, copper, and rubber being released into the system due to corrosion and wear in general. Additionally, the dry system was contaminated with small amounts of NP after the previously failed NF test. Due to the mix of particles present in the water, the material of the solid particles was selected as default for the SLS analysis (when using the Malvern Mastersizer 2000), which makes the reliance on the results debatable. To elaborate, when analyzing a sample in Malvern Mastersizer 2000, one must select the solid particle material. As the tap water consisted of multiple types of particles, default (standard) was chosen.

Figure 5.2 shows the PSD of the tap water from the erosion set-up before the addition of NF. The plot reveals the particle size ranging mostly from 0.3 to 1.0 μm. This appears to be mostly residual TiO_2 NP's which have agglomerated.

The following figure (Figure 5.3) displays the PSD of the operating NF before and after the erosion test. Both samples are shown to have particle sizes of nanometer-range, with a shift towards left for the sample after terminating the test. The size range is mainly from 300 to 1000 nm. The nanometer-range of the particles of both NF samples is an interesting finding, as the mixture was added directly into the tank, without prior ultrasonication.

The sample withdrawn before starting the erosion test can be seen in Figure 5.4, which

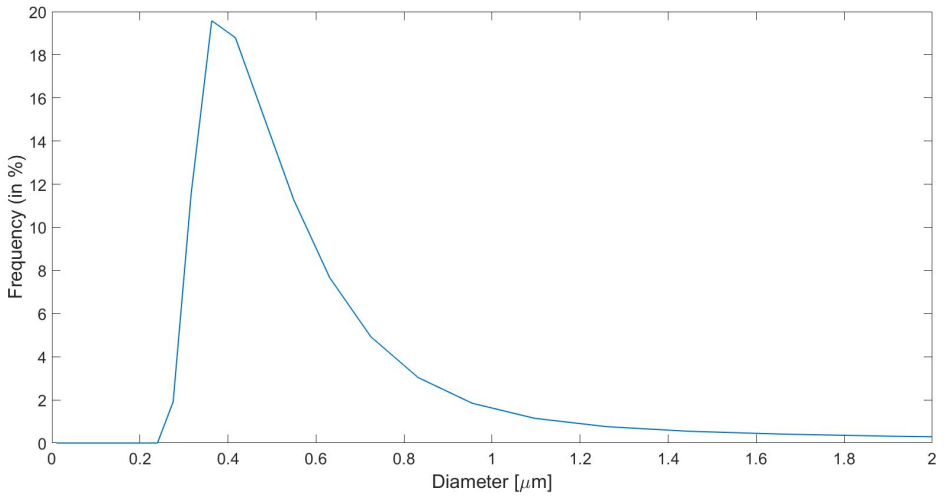

Figure 5.2: Normalized number frequency PSD of the contaminated tap water contained in the set-up

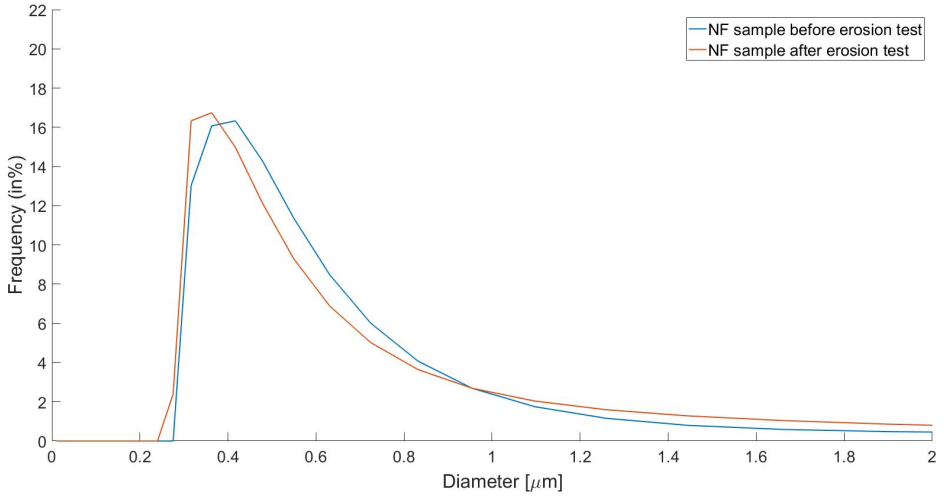

Figure 5.3: Normalized number frequencies of the NF at start and at the end of the erosion test.

illustrates the instability of this fluid. A fluid sample was also taken after the erosion test, and it looked nearly identical in terms of stability. There are separate layers of water and NP's, and nearly all NP's have precipitated.

The PSD data suggest that the circulation of the NF does not create significant amounts of agglomerates. By comparing the data in Figure 5.1 to that of Figure 5.3, one can observe that the operating fluid contains smaller particles than the 5 L sample. This result is interesting because it suggests a possible application for TiO_2-water NF's in systems where they are being stirred or are circulating. The deposition of the largest particles is a possible explanation for the shift towards left for the PSD after the NF test. It is also

Figure 5.4: Nanofluid collected after 96 hours (before erosion test).

to be noted that the sample was taken approximately in the middle of the tank, as it is not possible to withdraw a sample from the bottom due to the sample holder. The fluid at a lower level possibly contains particles of larger size. On the other hand, the outlet of the tank is at the bottom, causing the withdrawal of the heaviest fluid and a resulting homogeneous operating fluid.

One of the main criteria for an operating nanofluid is good stability, and the resulting erosion rates of this work are dependent on this quality. Yet, the final, unstable NF used in this work might not be a significant issue. While the erosion setup was running, the fluid was observed as a homogeneous fluid, and the presence of impinging NP's onto the target materials is roughly the same as if it would have been a stable fluid from the start. Additionally, if the operating fluid was a NF manufactured with 1.33 wt%, its stability could still be reduced due to circulation in the system. This assumption is supported by research finding the increased rate and intensity of collisions in a fluid to create larger agglomerates [70]. On the other hand, the opposite result was observed by Ediriweera et al. [20]. They investigated the reduction in particle size during an impact erosion test. Particle size was found to decrease, and larger particles were broken up more than the smaller particles. The large difference in kinetic energy pre- and post-collision breaks up particles, and kinetic energy is more sustained for bigger particles. Research by Austin [5] supports this information, which found that smaller particles usually require higher stress to break than larger particles.

The dilution of the NF concentration also affected by the stability of the fluid. The original NF (1 L sample) contained particles of 20 nm size, while the particles was of

$\sim$ 400 nm in the diluted fluid. This is contrary to previous research where increased concentration was found to promote agglomeration [49][74]. Fedele et al. [21], however concluded nanoparticle size to be independent of concentration.

Another aspect to take into consideration is the temperature increase during the erosion test. When terminating the experiment, the thermometer read a temperature of 63.2°C. It is of great interest to determine if temperature affects the agglomeration of NF's. A study by Witharana et al. [84] found TiO_2 NF particle size to be independent of a threefold temperature increase up to 60°C.

An additional important observation made from these plots is the shape of the size distributions; the plots are not symmetrical so none of them follows a normal distribution. Yet all are of the same shape.

Finally, it is to be noted that the changing surface of the eroded targets might affect the impact of the particles, and hence the split of the agglomerates. Especially work hardening of the surfaces can possibly enhance the degradation of particles [20].

5.1.2 The Mass of Target Materials

The main source of erosion data is based on the mass loss of the material targets. Before starting experiments with water, the nine target samples were weighed using Sartorius CPA 324S weight scale with an uncertainty of ±0.1 mg. The samples were weighed before and after both water tests and the NF test. This way one was able to compare the degree of erosion for water and NF as operational fluids.

The comparison of the weights of the specimen before and after impingement helps to measure the weight loss which is a measure of the rate of erosion.

The initial masses, in addition to the masses after experiments conducted with water and NF, can be found in Table 5.1. The remaining mass "data" can be found in Appendix A. Appendix A contains additional information about the masses after terminating the various tests and before drying the samples. The most relevant masses are found in Table 5.1.

Table 5.1: Mass loss measurements

		Initial mass [g]	**After first water test (time: 696 h) [g]**	**After second water test (time: 1008 h) [g]**	**After NF test (time: 336 h) [g]**
Plastic	#1	1.7142	1.7287	1.7849	1.7805
	#2	1.7065	1.7215	1.7576	1.7527
	#3	1.7343	1.7487	1.7631	1.7558
Rubber	#1	1.5504	1.7042	1.9566	2.0340
	#2	1.5439	1.6909	1.9575	2.0284
	#3	1.5436	1.6957	1.9615	2.0188
Copper	#1	10.7144	10.7103	10.6996	10.6929
	#2	10.5033	10.4970	10.4809	10.4736
	#3	10.3630	10.3580	10.3568	10.3494

Further, the mass data were treated to find the mass loss per unit time. These numbers can be found in Table 5.2. Interesting and somewhat unexpected results can be found. To begin with, all three rubber targets encountered a mass increase from the erosion test, and with similar rates for both operational fluids. The mass increases of the rubber targets were also visually observed, as the diameter of the targets had encountered an enlargement during the very first water test. The mass increase is believed to be caused by the absorption of particles (aluminum, copper, etc.) to the specimens. Natural rubber is known to have tack. By definition, tack is the energy required to separate two materials arranged in contact under moderate pressure for a short time [83]. This means it can adhere to itself in addition to other materials. In total, the results imply that the adhering properties of rubber outgo its somewhat "soft" hardness, which makes it sensitive to erosion.

The mean mass loss for every erosion test can be found in Table 5.3.

Table 5.2: Mass "change" rate (+ indicating mass increase, - indicating mass decrease)

		During first water test [g/yr.]	**During second water test [g/yr.]**	**During NF test [g/yr.]**
Plastic	#1	+ 0.182	+ 0.488	- 0.115
	#2	+ 0.189	+ 0.314	- 0.128
	#3	+ 0.181	+ 0.125	- 0.190
Rubber	#1	+ 1.936	+ 2.194	+ 2.020
	#2	+ 1.850	+ 2.317	+ 1.848
	#3	+ 1.914	+ 2.310	+ 1.494
Copper	#1	- 0.0516	- 0.0930	- 0.175
	#2	- 0.0793	- 0.1401	- 0.190
	#3	- 0.0629	- 0.0104	- 0.193

Table 5.3: Mean mass change of the three tests

	During first water test [g/yr.]	**During second water test [g/yr.]**	**During NF test [g/yr.]**
Plastic	+ 0.184 ± 0.004	+ 0.31 ± 0.15	- 0.14 ± 0.03
Rubber	+ 1.90 ± 0.04	+ 2.27 ± 0.06	+ 1.8 ± 0.2
Copper	- 0.646 ± 0.011	- 0.08 ± 0.05	- 0.186 ± 0.008

As for the plastic targets, a mass increase was observed for each target after both water tests, while a mass loss was encountered after the NF erosion test. Hence, the presence of solid NP seems to cause degradation at a small rate. However, the encountered mass increases of the two first tests are particularly interesting as PVC is a rigid material with high hardness. There is a possibility of particles adhering to its surface at first, and that impinging NP's remove them. The mean mass loss rate for plastic targets was 0.14 g/year, which is approximately a tenth of the observed rate of George et al. [24], who used aluminum and cast iron as target materials. Existing experimental research on the erosive effects of nanofluids have not studied target materials other than metals, reducing the ability to compare the resulting values of plastic.

The copper targets did on the other hand encounter a mass loss for all erosion tests. As seen in Table 5.2, there are differences between the erosion rates of water and NF as operational fluid. Especially, the rates of the first water test and the NF test deviates from each other. The mean erosion rate of the NF test is approximate twice the erosion rate of the water test. Results do however not indicate severe damage to the material; a degradation rate of $1{\cdot}10^{-5}$ g/hr results in a copper target of 10 g to take 114 years to fully degrade. This rate is in the same range as reported by Nguyen et al. [46], who found a mass loss rate of $7.778{\cdot}10^{-5}$ g/hr for alumina NF onto an aluminum surface. Celata et al. [10] investigated the erosive effects of TiO_2 onto a copper target, but found negligible erosive rates, which is also the case for this study.

Finally, it is also of interest to take into account the fluid temperature effect on erosion

rate. At the finalization of the NF test, the NF had reached a temperature of 63.2°C. Previous research observed different effects of temperature rise. Smeltzer et al. [72] found temperature increase to lower the erosion rate, while Coker et al. [16] experienced the opposite, with an erosion rate enhancement for temperatures up to 60°C, where it stagnated.

5.1.3 Wear Track Analysis by SEM

The following section focuses on the analysis of SEM images that can be directly used for observation of the wear of the surfaces. The first images were taken after the first erosion test conducted with water. New images were taken after the NF erosion test. It is to be noted that this section is only moderately elaborated, as it is not the main emphasis of this work. This work emphasizes the fluid dynamics of the erosive wear, not the material properties and the tribology aspect of it.

One target was selected for each material, and the images were taken with 1000, 5000 and 10 000 order of magnitude. The images contain information about the surface topography, so that the samples can be visually examined to find fractures and patterns of the material surfaces.

Figure 5.5a and 5.5b show the SEM images of surfaces of copper at a magnification of 1000x. By examination of the surfaces one notices larger pits in Figure 5.5b, which is evidence of wear. Most pits are of 5 μm diameter, which is larger than the mean size of NP's (400 nm) detected in the SLS analysis. It may seem as the eroding particles fracture the upper surface, and the resulting fracture gets infiltrated even further. The whirling pattern of the surface still exists, but the surface seems to have been worn down. There are also signs of a generally rougher surface in the post-erosion test. Additionally, there are no visible particles attached to the surface. The images support the mass loss found in Section 5.1.2. It is also important to note that the crater may also be caused by pitting corrosion, as this is common for copper in aggressive environments. The craters are more visible at a 10000x magnification, (see Figure 5.6).

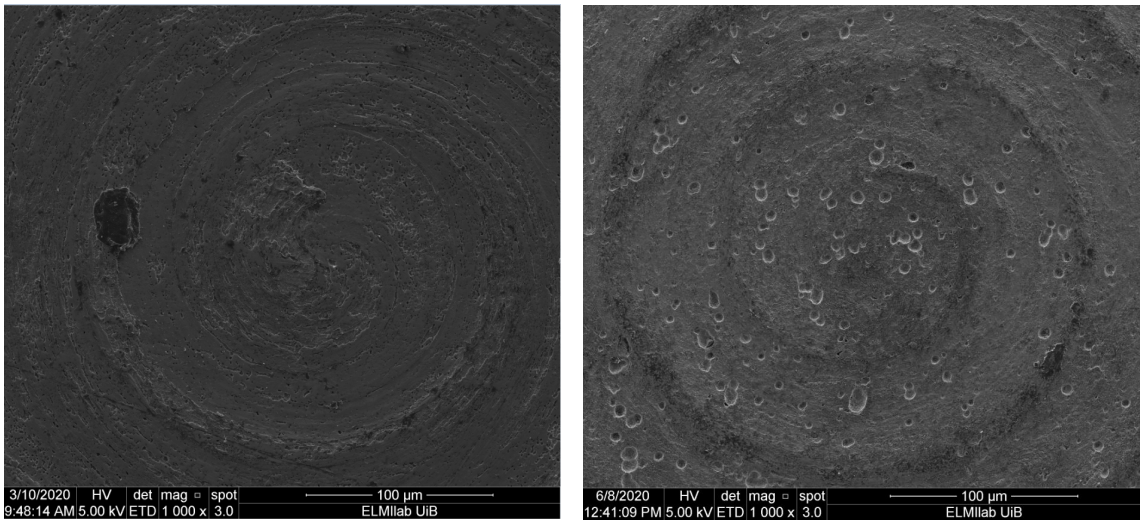

(a) Initial surface. (b) Surface after a total of three erosion tests.

Figure 5.5: SEM images of a copper target.

Pitting is a common corrosion wear mechanism, which leads to the formation of holes in the metal [56]. Our research can be compared to results from literature [40], which

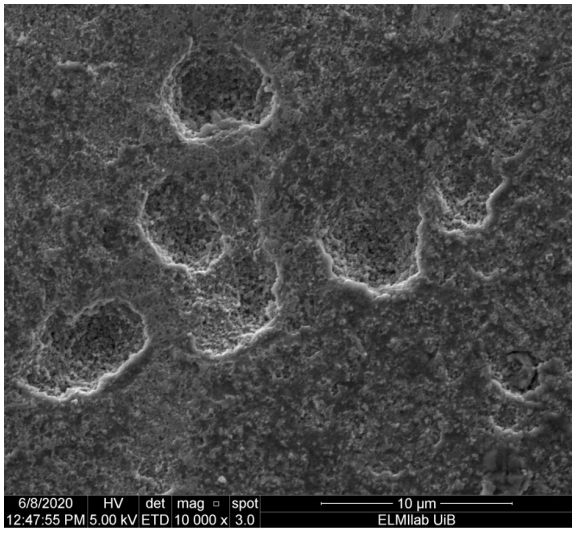

Figure 5.6: Copper surface at 10 000x magnification.

found galvanic pitting of a metal (see Figure 5.7). The pits visible in our SEM results are almost perfect circles, while the shapes in Figure 5.7 are irregular. Nonetheless, there is a resemblance between the pattern of this image and Figure 5.6. Hence, there is a possibility of corrosion contributing to the total wear of the copper surface. Additionally, the corrosion occurring during this research was flow-assisted, which increases the rate of attack on the metal. As there are NP's present in the operating fluid, the mechanism is a hybrid of erosion and corrosion. Erosion-corrosion produces holes that are all oriented to the flow pattern. This fact is also seen in the SEM images. If the wear is purely due to galvanic corrosion or erosion-corrosion is difficult to establish, but the presence of NP's enhances the probability that this phenomenon did occur. Experimental work has found erosion-corrosion to cause more material loss than pure erosion and corrosion [57][58].

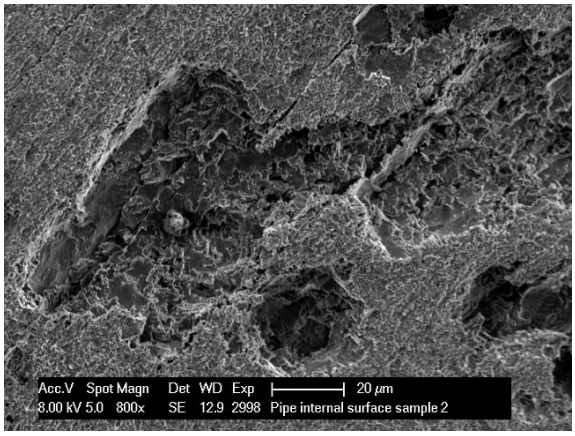

Figure 5.7: Pitting corrosion of a metal surface [40].

The difference in the surface structure of a plastic target before and after the erosion tests is exhibited in Figure 5.8a and 5.8b. Figure 5.8a displays a fracture of the plastic surface, which may give the impression that the surface is generally rough. Yet, one can observe the rest of the surface to be of finer structure. The post-NF test surface (Figure 5.8b) shows a more coarse surface for the entire section, which illustrates the mass loss described in section 5.1.2. The average distance between the ridges is 5 μm.

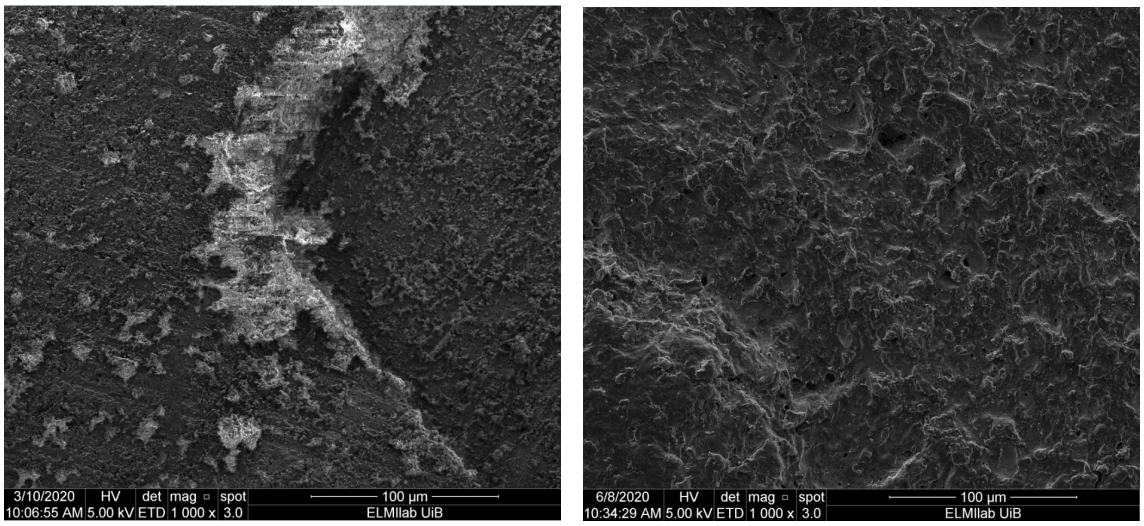

(a) Initial surface.

(b) Surface after a total of three erosion tests.

Figure 5.8: SEM images of a plastic target

The rubber target pre-erosion test (Figure 5.9a) shows a fairly smooth surface. A few fractures and some particles adhering to the surface can be detected. The particles are possibly aluminum or copper. The SEM image of the surface after the NF erosion test can be seen in Figure 5.9b. A visual examination of the image shows a reduced number of particles adhering to the surface. Additionally, the present particles are of much smaller size. The largest detectable particle, localized a bit left from the center, has a 5μm diameter. A uniform, more coarse surface throughout the sample can also be observed. The adhering particles could be detected by X-ray imaging, but it was not done due to the lack of time.

Altogether, the three materials did all obtain more coarse surfaces after the NF erosion test. Yet, this seems to be caused by different wear mechanisms based on the surface material and its properties. While plastic and rubber encountered a more uniform, rough wear, the copper surface got a quite smooth surface except for the significant amount of pitting.

Another element to consider is the time/day the SEM images were taken. The original plan was to get SEM images of the samples between the second water test and the NF test, but due to covid-19, this was not possible. Hence, there is no SEM image validating the wear after the second water test. It is therefore challenging to determine if the wear of the copper targets occurred mainly during the second water test or the NF test. This also

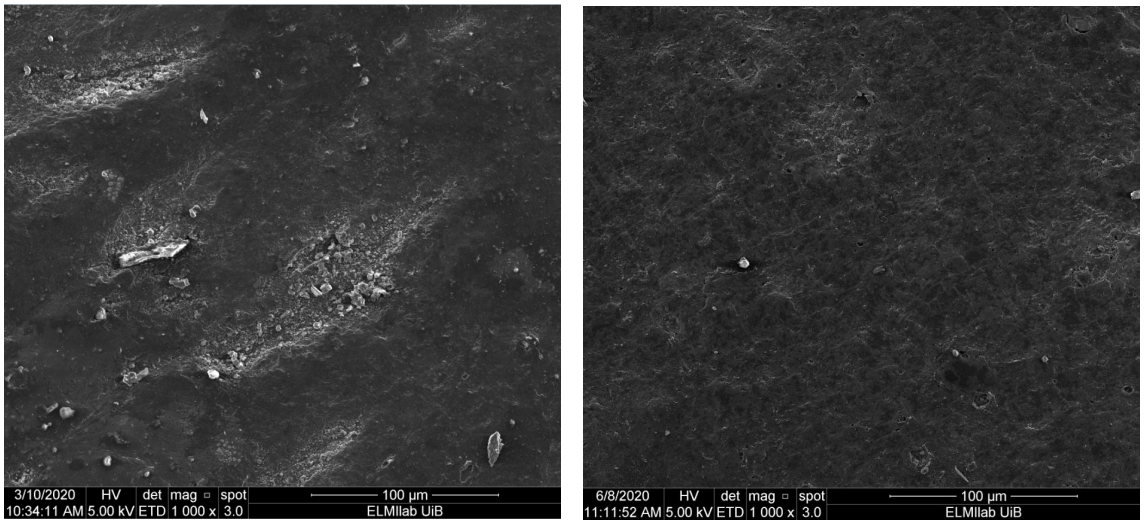

(a) Before (b) After

Figure 5.9: Rubber target before and after erosion tests.

affects the determination of which wear mechanism caused the pitting; was it corrosion alone or erosion-corrosion (with NP's present). If water alone causes galvanic pitting, the pitting holes would have been visible in the initial images. Additionally, there was a significant increase in the mass loss rate from the water tests to the NF test (as seen in Table 5.2). To sum up, most findings validate erosion-corrosion, and especially galvanic pitting corrosion as the main wear mechanism of the copper surface.

The eroded surfaces of rubber and plastic can be further examined in Figure 5.10 and 5.11, and they support the previously discussed topography of the targets. These are of 5000x magnification, and especially the rubber surface image (Figure 5.10) reveals cracks at multiple positions. It also becomes clearer that the plastic surface obtained the most coarse surface.

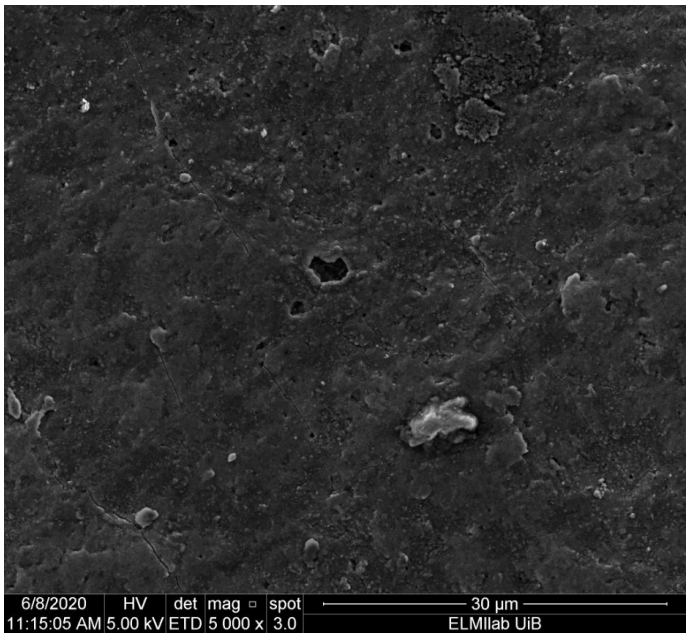

Figure 5.10: Rubber surface at 5000x magnification.

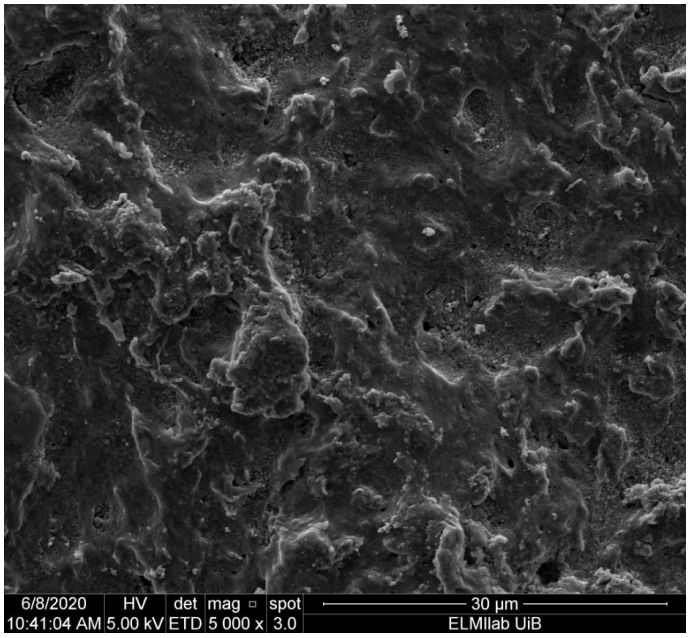

Figure 5.11: Plastic surface at 5000x magnification.

5.2 Numerical Investigation of Erosion Rate

The following section presents the results from the simulations performed in STAR-CCM+. Different parameters were changed to investigate their influence on the erosion rate. These parameters include particle density, particle size, and injector velocity.

5.2.1 Erosion Rate as a Function of Particle Material Density

First, simulations were conducted with a focus on particle density. The densities were selected from 1000 kg/m^3 to 10 000 kg/m^3 as most nanoparticles have densities of this range. The other properties of the dispersed phase were kept constant, as seen in Table 5.4.

Table 5.4: Conditions for density simulations

Property	**Value**	**Unit**
Inlet velocity, V_0	1.0	m/s
Particle diameter, d_p	$1{\cdot}10^{-7}$	m
Mass flow rate, $\dot{m}$	1.0	kg/s

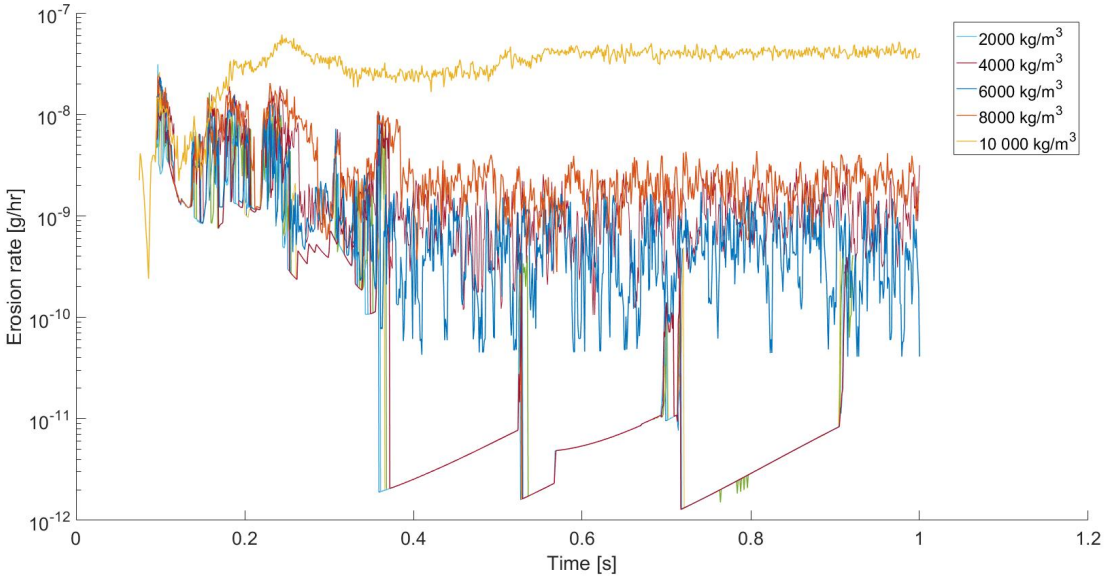

Figure 5.12: History of erosion rate for particles of densities from 2000 kg/m^3 to 10 000 kg/m^3

Figure 5.12 displays the range of the erosion rates. Except for the particles of 10 000 kg/m^3 density, all erosion rates are in the range of 10^{-10} to 10^{-8} g/hr. Vertical lines are also observed for the lowest density values, and they are occurring at a seemingly regular time-span. Nonetheless, a general trend can be observed; namely an increasing erosion rate with increasing particle density. Density is related to impact energy, which is one of the main contributors to erosion.

5.2.2 Erosion Rate as a Function of Injection Velocity

The erosion rate was investigated with various injection velocities ranging from 0.0 to 1.0 m/s. These velocities were selected as they are following the outlet velocity of the nozzle in the experimental investigation, as found in Section 4.1.4.1. The other injector properties were kept constant and can be seen in Table 5.5.

Table 5.5: Conditions for velocity simulations

Property	**Value**	**Unit**
Particle material density, ρ_d	4260	kg/m^3
Particle diameter, d_p	$1{\cdot}10^{-7}$	m
Mass flow rate, $\dot{m}$	1.0	kg/s

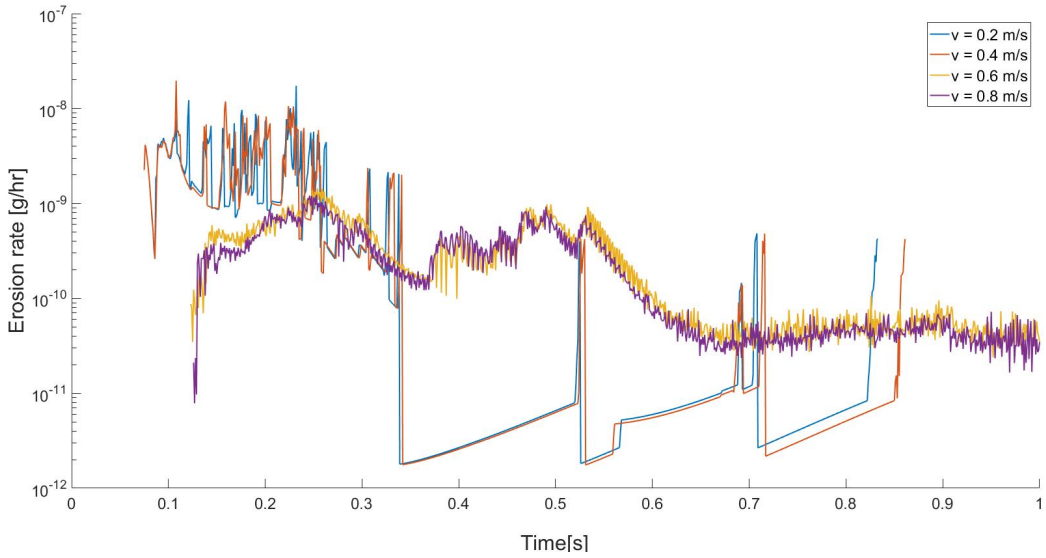

Figure 5.13: History of erosion rate as a function of outlet velocities

Figure 5.13 illustrates the effect of injection velocities selected as 0.2, 0.4, 0.6, and 0.8 m/s on predicted erosion rate. The graphs can be categorized into two groups as they follow each other closely. Velocities of 0.2 and 0.4 m/s are grouped, and so are the velocities 0.6 and 0.8 m/s. One can observe a large variation in erosion rates. Firstly, the values range from 10^{-8} to 10^{-12} g/hr. Additionally, the rates did not stabilize after $\sim$ 0.2 s as did the erosion rates investigating density and diameter. There are large variations in the shape of the graphs, and they do not follow any pattern, except for a decrease with time. The figure also indicates the erosion rate to increase with increasing injector velocity. A higher injection velocity results in higher impact energy which causes an enhanced erosion rate. This expected coherence is supported by numerous CFD [36][88] and experimental [33][39] research.

5.2.3 Erosion Rate as a Function of Particle Diameter

Particle diameter is an important characteristic that affects erosion magnitude. Erosion is proportional to kinetic energy, which is important for the impact and possible wear caused by the flow onto the surface.

When analyzing the effect of particle size on the erosion rate, the particle size range was selected as 1-500 μm. Larger ranges were tested at first, especially in the nanometer-range, but such small diameters caused negligible erosion rates. Additionally, at the start of this work, nanofluids were believed to agglomerate when applied to a circulating system, hence making the erosive rates of micro-meter sized particles relevant.

The other injector conditions were kept constant, and can be seen in Table 5.6.

Table 5.6: Conditions for particle diameter simulations

Property	**Value**	**Unit**
Inlet velocity, V_0	1.0	m/s
Particle material density, ρ_d	4260	kg/m^3
Mass flow rate, $\dot{m}$	1.0	kg/s

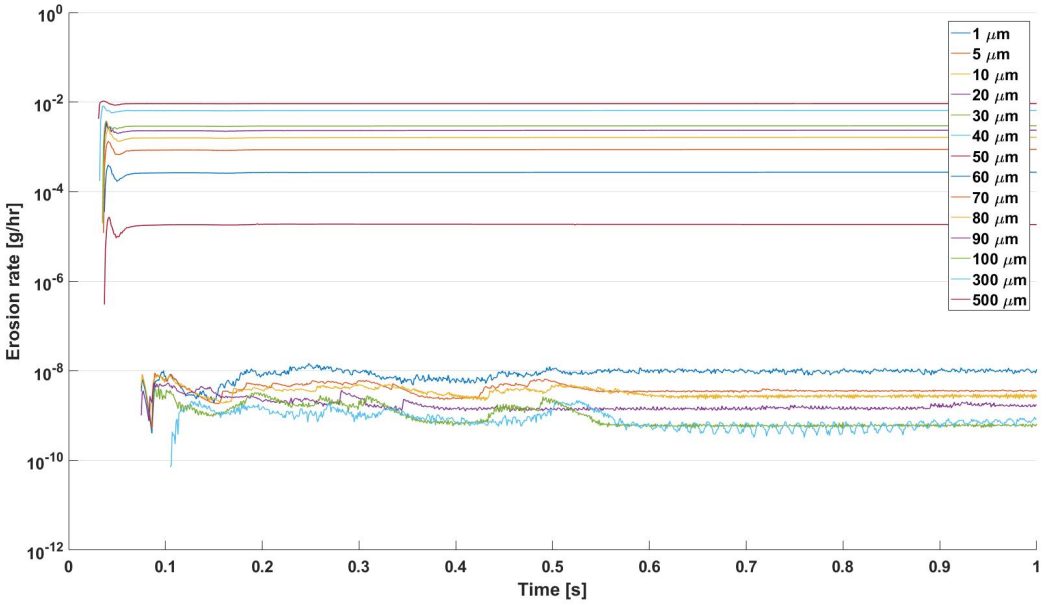

Figure 5.14: History of erosion rate from particles of various diameters.

Figure 5.14 represents all data found for the diameter-based simulations. This plot is difficult to analyze visually due to the many graphs, but it is included to show the gap from 10^{-5} to 10^{-8} g/hr. It is interesting how a 10 μm change in particle diameter results in such a large gap. Nonetheless, the low erosion rates observed for the particles of 1 to

40 μm can be due to numerical errors in the calculations, which limits their liability. Such low erosion rates imply no practical erosion.

The upper data series of the gap is 50 μm, and the lower limit is 1 μm, which is unexpected. There is a difference in the changing nature of erosion rate concerning particle diameter for the upper and lower group of the gap. For the upper group, the erosion rate seems to decrease at an even rate for lowered particle diameter. On the contrary, the erosion rate increases for lowered particle diameter for the bottom group. Hence, the lowest erosion rate observed for this group is for 40 μm, while the largest is observed for 1 μm. The steady erosion rate at $\sim 1{\cdot}10^{-8}$ g/h for diameters of 1 μm corresponds to a yearly rate of $8.76{\cdot}10^{-5}$g. This value is less than a thousandth of the experimentally obtained mean value of 0.163 g/year.

Still, the erosion rates in the range of 10^{-5} to 10^{-2} g/h illustrate erosion rate as proportional to particle size. Tilly [77] reports the same proportionality for particles over 100 μm. Other research has also found increasing particle size to enhance erosion rate [15][48].

There seems to be a critical diameter between 40 and 50 μm. As seen in Figure 5.15, the erosion rates of particles less than 40 μm have values ranging from 10^{-9} to 10^{-8} g/h. At such low values, there is a large probability of numerical errors. Figure 5.15 shows the erosion rate of 1 μm particles is higher than that of 40 μm. Erosion rates were also found to increase for decreasing particle sizes in other research [23].

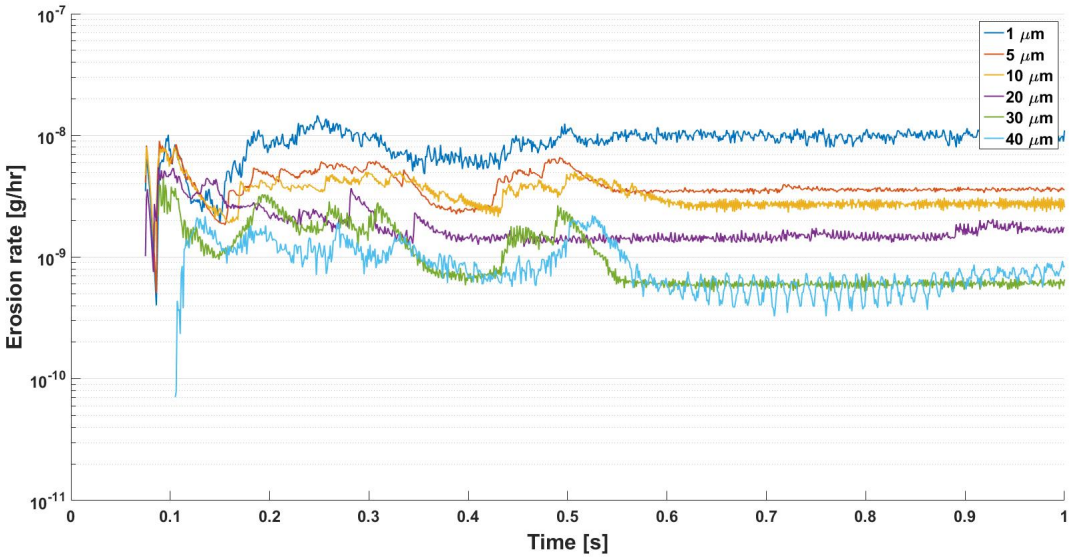

Figure 5.15: History of erosion rates for particles of small diameters

Figure 5.14 displays that the erosion rates become steady shortly after start. A steady value for the erosion rate was selected at 1 s for each particle diameter. The extracted data was plotted in Figure 5.16. From this plot, it becomes more evident that there exists a shift in the erosion rate trend at around 40 μm. Other research have also observed an

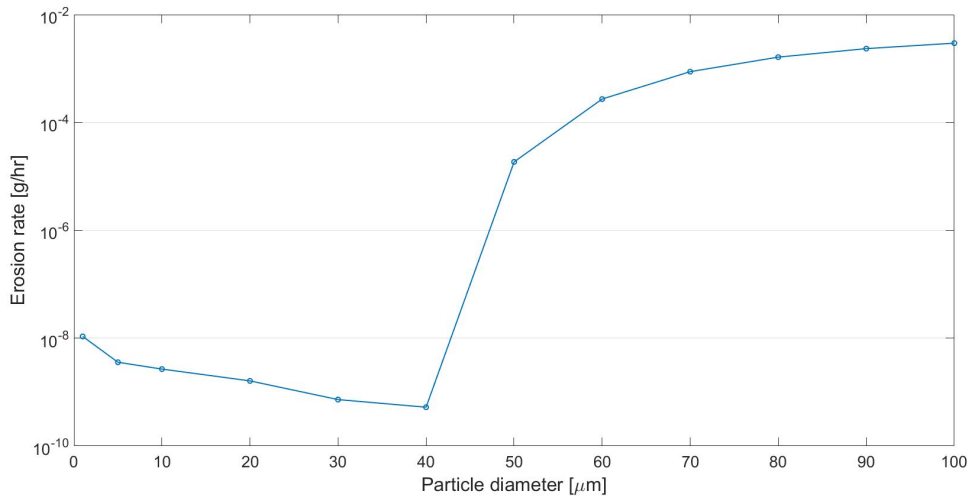

Figure 5.16: Steady erosion rates for particles of different diameters.

extremum of erosion rate for a range of particle diameters, but most of these involve a maximum erosion rate [38][48].

An important aspect to consider with the simulation results is the fact that the mass flow rate was kept constant. This means that a reduction in particle diameter increases the number of particles present in the fluid stream. Yet, it seems like the larger number of particles present does not atone for the smaller kinetic energy of each particle. This phenomenon does not affect the erosion behavior of the smaller particles significantly, which can be understood by the fact that the increased number of particles present in the flow does not mean that they hit the target surface. There are rebounding particles present at the surface deflecting impinging particles. Furthermore, the particles need a critical amount of kinetic energy to penetrate the surface and remove surface material. This supports our results of finding a reduction in erosion rate for smaller particles.

Figures 5.17 (a-d)) illustrate the surface of the eroded target. An observation was made; the eroded area shifts location from right below the nozzle outlet to outside the center at a certain particle diameter. It is highly interesting how a decrease in particle diameter and consequently, erosion rate, leads to a redirection of the fluid stream direction and hence the eroded area.

This observation may be explained by the fact that smaller particles are affected by the fluid at a larger degree. A numerical study by Aponte et al. [3] explained this as the smaller particles follow the fluid stream, even after impingement, while larger particles (due to their bigger inertia and drag) follow the conditions defined by the nozzle outlet. This can be explained by the difference in momentum response time, and smaller particles are more easily swept out of the target center and cause erosion at outer locations and at a lower impact angle.

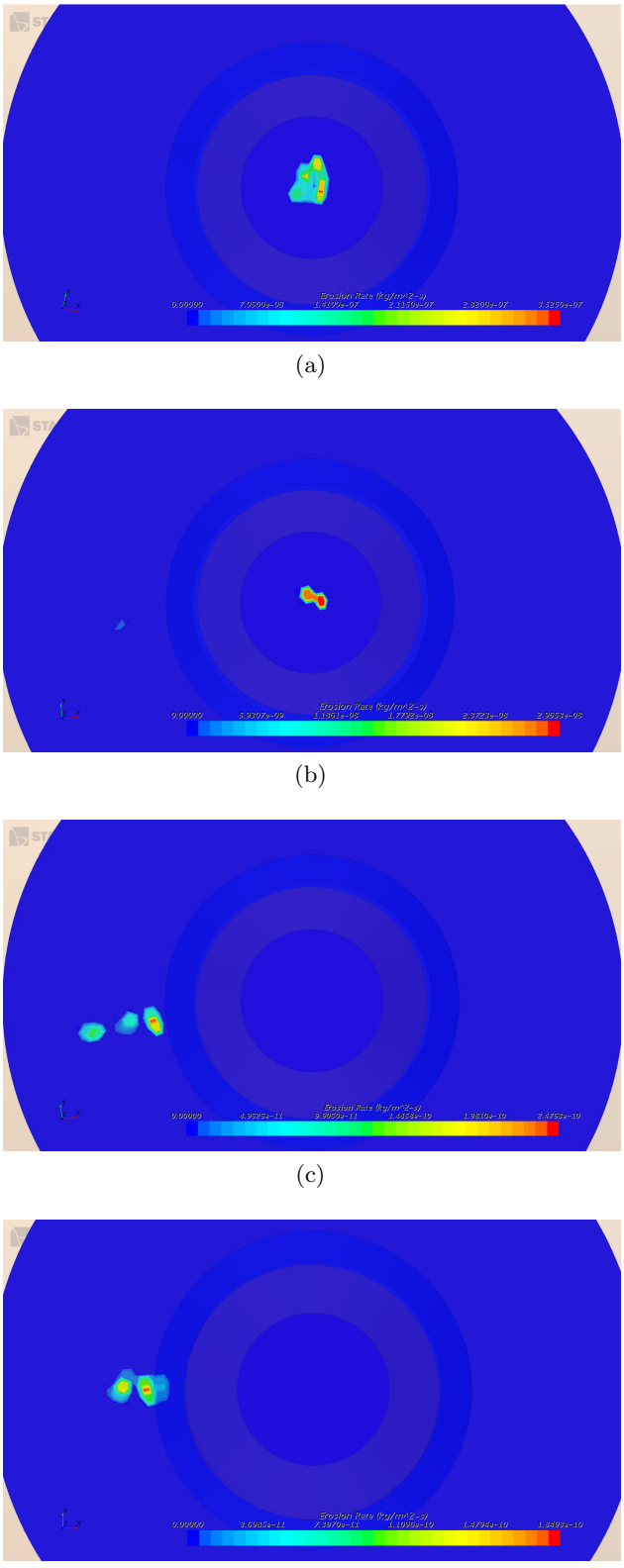

(a)

(b)

(c)

(d)

Figure 5.17: Erosion fields for various diameters at 1 s. From top to bottom:(a) 45 μm, (b) 42 μm, (c) 40 μm, and (d) 30 μm.

A closer image of the erosion field can be seen in Figure 5.18. Here one can study the pattern of the eroded area, which reveals a low erosion rate in the middle of the field, with an increasing rate around it. This can be described as a W-pattern if it were seen horizontally onto the intersection. The point in the middle is called stagnation point, with high velocity region outside. This can be seen in Figure 5.19. W-patterns has been observed in previous work of solid-liquid streams in direct impingement geometries, both experimental [48][81] and numerical [25][42][47]. It is important to note that the W-pattern occurs on target surfaces submerged in liquids.

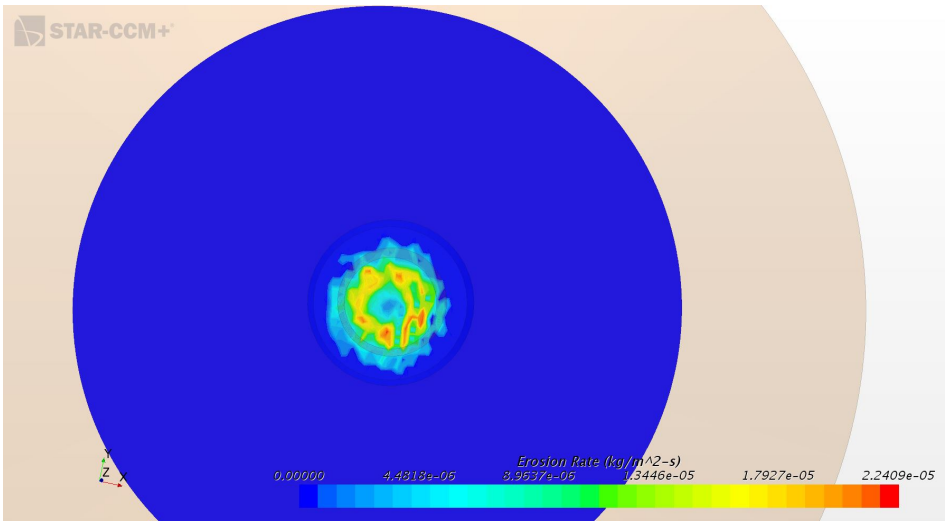

Figure 5.18: The pattern of an eroded field for a particle diameter of 70 μm.

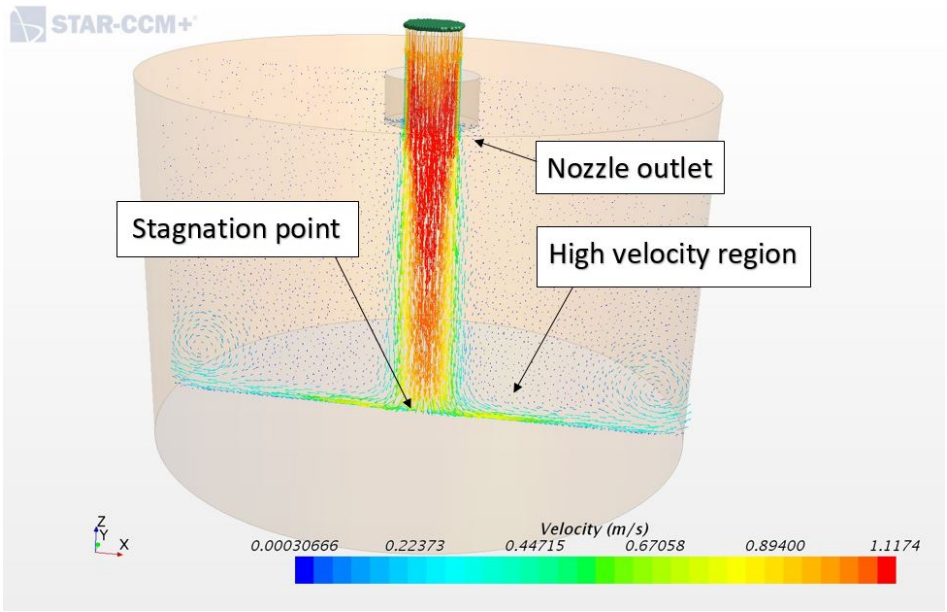

Figure 5.19: Velocity stream contour of the multiphase flow.

5.3 Comparison of the Experimental and Numerical Results

Both employed methods of this research resulted in low erosion rates. The mean erosion rates for plastic and copper during the experimental NF test were 0.14 ±0.03 g/year and 0.186 ±0.008 g/year, respectively. The particle size of the operating fluid of this test ranged from 300 nm to 1 μm. Only one of our simulations were done in this size range, namely the test for 1 μm. From this simulation, a steady erosion rate was obtained with a value of $9.424 \cdot 10^{-5}$ g/year.

The true particle size range of the operating NF is possibly larger than the values obtained from the SLS analysis due to sedimentation. The numerical investigation did obtain erosion rates in the same range as the experimental values, but these are for particle sizes larger than 70 μm. It is doubtful to assume that the NF particle size was of such large diameter, especially the ones in circulation.

Another element to consider is the injection velocity. In the experimental test, the flow rate was observed in the range of 0.19 m^3/h to 0.23 m^3/h. This results in nozzle outlet velocities from 0.83 m/s to 1.0 m/s. The simulations investigated the erosion rate for particles of 100 nm at a 0.8 m/s injection velocity. The resulting steady erosion rate was in the range of $1 \cdot 10^{-11}$ g/hr, which corresponds to a rate of $8.8 \cdot 10^{-8}$ g/year. To summarize, particle size-dependent, density-dependent, and velocity-dependent simulations obtained erosion rates deviating significantly from the experimentally obtained erosion rate.

Although CFD is an excellent tool for predicting real-life situations, it does encounter certain limitations. It should be emphasized that the employment of CFD in this research was conducted to get a qualitative description of the process, and not to copy the experiment. In the case of this work, there are particular elements of the experimental test which STAR-CCM+ does not take into account. To begin with, STAR-CCM+ does not account for the target material; there is a default one used for all erosion modeling. Although the applied Oka model uses constants based on target material properties, they are already given when this model is selected. Additionally, the turbulent modeling has been selected for simulations, which might not be the case as the nozzle outlet velocity and nozzle diameter of the experiment are of low values.

Chapter 6

Concluding Remarks

In this research, both an experimental and a numerical method was applied to investigate the erosive effects of a solid-liquid flow onto a flat target.

For the experimental investigation, an erosion set-up was developed to expose submerged targets to a low-speed impinging TiO_2 NF. The operating NF had a concentration of 1.33 wt.%. The target materials were circular slices of rubber, copper, and plastic (PVC). The test duration of the NF impingement was selected as 336 hours. SEM images and weighing of the targets were chosen to examine the possible erosion. Firstly, SEM images were taken before and after the erosion test for comparison. The post-test images suggest general wear occurring to the selected material surfaces. Significant wear was observed for the copper targets, in the form of erosion-corrosion.

As for the weight difference of the material targets, the target materials experienced a different outcome. Foremost, the rubber targets encountered an unexpected mass increase. As regards the plastic and copper, a mass decrease was discovered. A mean mass loss rate was found as 0.144 g/year and 0.186 g/year for plastic and copper targets, respectively. Plastic target mass loss was identified to be caused by erosion, while the copper wear was identified as mostly galvanic corrosion.

Additionally, SLS investigations were conducted for the operating NF to study the effect circulation and time have on the stability of the employed NF. A test duration of 336 hours in a circulating system found the PSD of the sample to shift towards left; meaning agglomerates were broken up and larger particles settled out. The results indicate particles of size 300 to 1000 nm to be present in the NF.

The numerical investigation was conducted in the CFD software STAR-CCM+ to get qualitative information on the erosion process at similar conditions as the experimental one. A multiphase flow of micrometer-sized particles in water impinged through a nozzle onto a flat target. Langrangian tracking was selected for the dispersed phase, and the Oka model [50] was selected for erosion modeling. The erosion rate of the target was investigated by the influence of particle diameter, velocity, and particle density. Increasing velocity and particle density was found to enhance the erosion rate. A more complex result was found

from the investigation of particle diameter. A diameter of ∼40 μm was identified to cause the lowest erosion rate for a particle diameter range from 1 to 500 μm, with an erosion rate of $4.59{\cdot}10^{-6}$ g/yr. Additionally, the erosion field location experienced a shift at this diameter. To elaborate, for every particle diameter larger than the critical diameter, the erosion field was observed at the centre of the target, but for particles of smaller size, the erosion field relocated further from the center.

Chapter 7

Future Work

There are numerous opportunities for further work. For this research, an experimental erosion set-up was used to investigate the erosive effects of NF's. The system needs refinement to investigate erosion alone. Primarily, the components of the system need to be changed to avoid corrosive effects. Additionally, an investigation is in order to find pumps better fitted to the use of NF's.

Suggestion for future work is listed below:

- Improvement of the already developed erosion set-up
- Develop erosion models implementing particle-particle interactions
- Appropriate relations for nanofluids should be provided for CFD codes
- Improve erosion prediction models and obtaining an accurate model applicable for an entire spectrum of conditions
- Investigate the stability and particle size distribution of NF's when implemented in circulating systems
- Develop an universal test rig for the erosion of NF's
- Obtain a better understanding of the corrosion involved in the wear caused by NF's
- Study the effect of changing the values of the Oka model coefficients
- Implement numerical erosion models other than the Oka model for comparison

Bibliography

[1] A. Akbarinia and A. Behzadmehr. "Numerical study of laminar mixed convection of a nanofluid in horizontal curved tubes". In: *Applied Thermal Engineering* 27.8-9 (2007), pp. 1327–1337.

[2] J.D. Anderson and J. Wendt. *Computational fluid dynamics*. Vol. 206. Springer, 1995.

[3] R.D. Aponte, L.A. Teran, J.A. Ladino, F. Larrahondo, J.J. Coronado, and S.A. Rodrıguez. "Reprint of "Computational study of the particle size effect on a jet erosion wear device"". In: *Wear* 376 (2017), pp. 526–532.

[4] M.J. Assael, I.N. Metaxa, J. Arvanitidis, D. Christofilos, and C. Lioutas. "Thermal conductivity enhancement in aqueous suspensions of carbon multi-walled and double-walled nanotubes in the presence of two different dispersants". In: *International Journal of Thermophysics* 26.3 (2005), pp. 647–664.

[5] L.G. Austin. "A treatment of impact breakage of particles". In: *Powder Technology* 126.1 (2002), pp. 85–90.

[6] A. Behzadmehr, M. Saffar-Avval, and N. Galanis. "Prediction of turbulent forced convection of a nanofluid in a tube with uniform heat flux using a two phase approach". In: *International Journal of Heat and Fluid Flow* 28.2 (2007), pp. 211–219.

[7] E. Bellos, Z. Said, and C. Tzivanidis. "The use of nanofluids in solar concentrating technologies: a comprehensive review". In: *Journal of Cleaner Production* 196 (2018), pp. 84–99.

[8] BP p.l.c. *BP Statistical Review of World Energy*. `https://www.bp.com/content/dam/bp/business-sites/en/global/corporate/pdfs/energy-economics/statistical-review/bp-stats-review-2019-full-report.pdf`. Online; accessed 30 May 2020. 2019.

[9] R. Bubbico, G.P. Celata, F. D'Annibale, B. Mazzarotta, and C. Menale. "Experimental analysis of corrosion and erosion phenomena on metal surfaces by nanofluids". In: *Chemical Engineering Research and Design* 104 (2015), pp. 605–614.

[10] G.P. Celata, F. D'Annibale, A. Mariani, S. Sau, E. Serra, R. Bubbico, C. Menale, and H. Poth. "Experimental results of nanofluids flow effects on metal surfaces". In: *Chemical Engineering Research and Design* 92.9 (2014), pp. 1616–1628.

[11] H. Chen, Y. Ding, Y. He, and C. Tan. "Rheological behaviour of ethylene glycol based titania nanofluids". In: *Chemical Physics Letters* 444.4-6 (2007), pp. 333–337.

[12] M. Chieruzzi, G.F. Cerritelli, A. Miliozzi, and J.M. Kenny. "Effect of nanoparticles on heat capacity of nanofluids based on molten salts as PCM for thermal energy storage". In: *Nanoscale Research Letters* 8.1 (2013), p. 448.

[13] S.U.S. Choi and J.A. Eastman. *Enhancing thermal conductivity of fluids with nanoparticles*. Tech. rep. Argonne National Lab., IL (United States), 1995.

[14] S.U.S. Choi, Z.G. Zhang, W. Yu, F.E. Lockwood, and E.A. Grulke. "Anomalous thermal conductivity enhancement in nanotube suspensions". In: *Applied Physics Letters* 79.14 (2001), pp. 2252–2254.

[15] H.M. Clark. "The influence of the flow field in slurry erosion". In: *Wear* 152.2 (1992), pp. 223–240.

[16] E.H. Coker and D. Van Peursem. "The erosion of horizontal sand slurry pipelines resulting from inter-particle collision". In: *Wear* 400 (2018), pp. 74–81.

[17] C.T. Crowe. *Multiphase flow handbook*. CRC press, 2005.

[18] Y. Ding and D. Wen. "Particle migration in a flow of nanoparticle suspensions". In: *Powder Technology* 149.2-3 (2005), pp. 84–92.

[19] J.A. Eastman, S.U.S. Choi, S. Li, W. Yu, and L.J. Thompson. "Anomalously increased effective thermal conductivities of ethylene glycol-based nanofluids containing copper nanoparticles". In: *Applied Physics Letters* 78.6 (2001), pp. 718–720.

[20] M. Ediriweera, J. Chladek, and C. Ratnayake. "Effect of impact angle, exposure time, and particle size on impact erosion". In: *Particulate Science and Technology* (2019), pp. 1–9.

[21] L. Fedele, L. Colla, and S. Bobbo. "Viscosity and thermal conductivity measurements of water-based nanofluids containing titanium oxide nanoparticles". In: *International Journal of Refrigeration* 35.5 (2012), pp. 1359–1366.

[22] L. Fuyan and S. Hesheng. "The effect of impingement angle on slurry erosion". In: *Wear* 141.2 (1991), pp. 279–289.

[23] W. Gao, Y. Li, and L. Kong. "Numerical investigation of erosion of tube sheet and tubes of a shell and tube heat exchanger". In: *Computers & Chemical Engineering* 96 (2017), pp. 115–127.

[24] G. George, R.K. Sabareesh, S. Thomas, V. Sajith, T. Hanas, S. Das, and C.B. Sobhan. "Experimental investigation of material surface erosion caused by TiO2 nanofluid impingement". In: *Journal of Nanofluids* 3.2 (2014), pp. 97–107.

[25] A. Gnanavelu, N. Kapur, A. Neville, J.F. Flores, and N. Ghorbani. "A numerical investigation of a geometry independent integrated method to predict erosion rates in slurry erosion". In: *Wear* 271.5-6 (2011), pp. 712–719.

[26] L. Godson, B. Raja, D.M. Lal, and S. Wongwises. "Enhancement of heat transfer using nanofluids—an overview". In: *Renewable and Sustainable Energy Reviews* 14.2 (2010), pp. 629–641.

[27] L. Godson, B. Raja, D.M. Lal, and S. Wongwises. "Experimental investigation on the thermal conductivity and viscosity of silver-deionized water nanofluid". In: *Experimental Heat Transfer* 23.4 (2010), pp. 317–332.

[28] J. Hinze. *0. 1975 Turbulence*. 1972.

[29] T.K. Hong, H.S. Yang, and C.J. Choi. "Study of the enhanced thermal conductivity of Fe nanofluids". In: *Journal of Applied Physics* 97.6 (2005), p. 064311.

[30] S.M. Hsu, M.C. Shen, and A.W. Ruff. “Wear prediction for metals”. In: *Tribology International* 30.5 (1997), pp. 377–383.

[31] A.M. Hussein, K.V. Sharma, R.A. Bakar, and K. Kadirgama. “The effect of nanofluid volume concentration on heat transfer and friction factor inside a horizontal tube”. In: *Journal of Nanomaterials* 2013 (2013).

[32] I. Hutchings and P. Shipway. *Tribology: friction and wear of engineering materials*. Butterworth-Heinemann, 2017.

[33] H. Jiang, W. Wang, D. Chu, W. Lu, D. Cheng, Y. Huang, and Y. Wu. “Corrosion-erosion tests of fusion reactor materials in flowing nanofluids”. In: *Journal of Nuclear Materials* 494 (2017), pp. 361–367.

[34] A. Kamyar, R. Saidur, and M. Hasanuzzaman. “Application of computational fluid dynamics (CFD) for nanofluids”. In: *International Journal of Heat and Mass Transfer* 55.15-16 (2012), pp. 4104–4115.

[35] K.M. Koczkur, S. Mourdikoudis, L. Polavarapu, and S.E. Skrabalak. “Polyvinylpyrrolidone (PVP) in nanoparticle synthesis”. In: *Dalton Transactions* 44.41 (2015), pp. 17883–17905.

[36] A. Kosinska, B.V. Balakin, and P. Kosinski. “Theoretical analysis of erosion in elbows due to flows with nano-and micro-size particles”. In: *Powder Technology* 364 (2020), pp. 484–493.

[37] Y. Li, S. Tung, E. Schneider, S. Xi, et al. “A review on development of nanofluid preparation and characterization”. In: *Powder Technology* 196.2 (2009), pp. 89–101.

[38] M. Liebhard and A. Levy. “The effect of erodent particle characteristics on the erosion of metals”. In: *Wear* 151.2 (1991), pp. 381–390.

[39] J. Liu, W. BaKeDaShi, Z. Li, Y. Xu, W. Ji, C. Zhang, G. Cui, and R. Zhang. “Effect of flow velocity on erosion–corrosion of 90-degree horizontal elbow”. In: *Wear* 376 (2017), pp. 516–525.

[40] LPD Lab Services. *Galvanic, Pitting and Crevise Corrosion*. Online; accessed 20 June 2020. 2020.

[41] A. Magnee. “Generalized law of erosion: application to various alloys and intermetallics”. In: *Wear* 181 (1995), pp. 500–510.

[42] A. Mansouri, H. Arabnejad, S.A. Shirazi, and B.S. McLaury. “A combined CFD/-experimental methodology for erosion prediction”. In: *Wear* 332 (2015), pp. 1090–1097.

[43] W.L. McCabe, J.C. Smith, and P. Harriott. *Unit operations of chemical engineering*. Vol. 7. McGraw-hill New York, 2005.

[44] G.J. Molina, F. Aktaruzzaman, K. Martin, V. Soloiu, and M. Rahman. “Testing of Wear and Erosion Effects of Nanofluids on Metals: New Instruments and Assessment Methodologies”. In: (2018).

[45] G.J. Molina, F. Aktaruzzaman, W. Stregles, V. Soloiu, and M. Rahman. “Jet-impingement effects of alumina-nanofluid on aluminum and copper”. In: *Advances in Tribology* 2014 (2014).

[46] C.T. Nguyen, G. Laplante, M. Cury, and G. Simon. “Experimental investigation of impinging jet heat transfer and erosion effect using Al2O3-water nanofluid”. In:

Proceedings of the 6th IASME/WSEAS International Conference on Fluid Mechanics and Aerodynamics (FMA'08). Citeseer. 2008.

[47] V.B. Nguyen, Q.B. Nguyen, C.Y.H. Lim, Y.W. Zhang, and B.C. Khoo. "Effect of air-borne particle–particle interaction on materials erosion". In: *Wear* 322 (2015), pp. 17–31.

[48] V.B. Nguyen, Q.B. Nguyen, Y.W. Zhang, C.Y.H. Lim, and B.C. Khoo. "Effect of particle size on erosion characteristics". In: *Wear* 348 (2016), pp. 126–137.

[49] E. Nourafkan, M. Asachi, H. Gao, G. Raza, and D. Wen. "Synthesis of stable iron oxide nanoparticle dispersions in high ionic media". In: *Journal of Industrial and Engineering Chemistry* 50 (2017), pp. 57–71.

[50] Y.I. Oka, K. Okamura, and T. Yoshida. "Practical estimation of erosion damage caused by solid particle impact: Part 1: Effects of impact parameters on a predictive equation". In: *Wear* 259.1-6 (2005), pp. 95–101.

[51] Our World in Data. *Global Primary Energy Consumption*. `https://ourworldindata.org/grapher/global-primary-energy`. Online; accessed 30 May 2020. 2018.

[52] S. Özerinç, S. Kakaç, and A.G. Yazıcıoğlu. "Enhanced thermal conductivity of nanofluids: a state-of-the-art review". In: *Microfluidics and Nanofluidics* 8.2 (2010), pp. 145–170.

[53] H.E. Patel, S.K. Das, T. Sundararajan, A. Sreekumaran Nair, B. George, and T. Pradeep. "Thermal conductivities of naked and monolayer protected metal nanoparticle based nanofluids: Manifestation of anomalous enhancement and chemical effects". In: *Applied Physics Letters* 83.14 (2003), pp. 2931–2933.

[54] G. Paul, T. Pal, and I. Manna. "Thermo-physical property measurement of nanogold dispersed water based nanofluids prepared by chemical precipitation technique". In: *Journal of Colloid and Interface Science* 349.1 (2010), pp. 434–437.

[55] J. Philip and P.D. Shima. "Thermal properties of nanofluids". In: *Advances in Colloid and Interface Science* 183 (2012), pp. 30–45.

[56] B.N. Popov. *Corrosion engineering: principles and solved problems*. Elsevier, 2015.

[57] A.M. Rashidi, M. Packnezhad, M. Moshrefi-Torbati, and F.C. Walsh. "Erosion–corrosion synergism in an alumina/sea water nanofluid". In: *Microfluidics and Nanofluidics* 17.1 (2014), pp. 225–232.

[58] A.M. Rashidi, M. Paknezhad, M.R. Mohamadi-Ochmoushi, and M. Moshrefi-Torbati. "Comparison of erosion, corrosion and erosion–corrosion of carbon steel in fluid containing micro-and nanosize particles". In: *Tribology-Materials, Surfaces & Interfaces* 7.3 (2013), pp. 114–121.

[59] A.V. Reddy and G. Sundararajan. "Erosion behaviour of ductile materials with a spherical non-friable erodent". In: *Wear* 111.3 (1986), pp. 313–323.

[60] Y. Ren and D. Jing. "Study on particle and photonic flux distributions in a magnetically stirred photocatalytic reactor". In: *Journal of Photonics for Energy* 5.1 (2015), p. 052097.

[61] O. Reynolds. "XXIX. An experimental investigation of the circumstances which determine whether the motion of water shall be direct or sinuous, and of the law of resistance in parallel channels". In: *Philosophical Transactions of the Royal society of London* 174 (1883), pp. 935–982.

[62] J. Routbort, D. Singh, E. Timofeeva, W. Yu, and R. Smith. "Erosion of radiator materials by nanofluids". In: *Argonne National Laboratory, Vehicle Technologies–Annual Review* (2010).

[63] J. Routbort, D. Singh, W. Yu, G. Chen, D. Cookson, R. Smith, and T. Sofu. "Effects of nanofluids on heavy vehicle cooling systems". In: *Proceedings of the VT Annual Merit Review Meeting*. Argonne National Laboratory. 2008, pp. 1–16.

[64] M.R. Safaei, O. Mahian, F. Garoosi, K. Hooman, A. Karimipour, S.N. Kazi, and S. Gharehkhani. "Investigation of micro-and nanosized particle erosion in a 90 pipe bend using a two-phase discrete phase model". In: *The Scientific World Journal* 2014 (2014).

[65] M.S. Saterlie, H. Sahin, B. Kavlicoglu, Y. Liu, and O.A. Graeve. "Surfactant effects on dispersion characteristics of copper-based nanofluids: A dynamic light scattering study". In: *Chemistry of Materials* 24.17 (2012), pp. 3299–3306.

[66] L. Schiller and A. Naumann. "A drag coefficient correlation". In: *Z. Ver. Deutsch. Ing* 77 (1935), p. 318.

[67] S. Sen Gupta, V. Manoj Siva, S. Krishnan, T.S. Sreeprasad, P.K. Singh, T. Pradeep, and S.K. Das. "Thermal conductivity enhancement of nanofluids containing graphene nanosheets". In: *Journal of Applied Physics* 110.8 (2011), p. 084302.

[68] F.S. Shariatmadar and S.G. Pakdehi. "Effect of various surfactants on the stability time of kerosene–boron nanofluids". In: *Micro & Nano Letters* 11.9 (2016), pp. 498–502.

[69] S.M. Shinde, D.M. Kawadekar, P.A. Patil, and V.K. Bhojwani. "Analysis of micro and nano particle erosion by the numerical method at different pipe bends and radius of curvature". In: *International Journal of Ambient Energy* (2019), pp. 1–8.

[70] S.W. Siddiqui, P.J. Unwin, Z. Xu, and S.M. Kresta. "The effect of stabilizer addition and sonication on nanoparticle agglomeration in a confined impinging jet reactor". In: *Colloids and Surfaces A: Physicochemical and Engineering Aspects* 350.1-3 (2009), pp. 38–50.

[71] Siemens PLM Software. *Simcenter STAR-CCM+ Tutorial Guide for version 13.06*. Online; accessed 15 June 2020. 2020.

[72] C.E. Smeltzer, M.E. Gulden, and W.A. Compton. "Mechanisms of metal removal by impacting dust particles". In: (1970).

[73] V. Smil. *Energy transitions: global and national perspectives*. ABC-CLIO, 2016.

[74] D. Song, M. Hatami, Y. Wang, D. Jing, and Y. Yang. "Prediction of hydrodynamic and optical properties of TiO2/water suspension considering particle size distribution". In: *International Journal of Heat and Mass Transfer* 92 (2016), pp. 864–876.

[75] *Static Light Scattering (SLS)*. `https://www.malvernpanalytical.com/en/products/technology/light-scattering/static-light-scattering`. Accessed: 2020-05-23.

[76] G. Sundararajan. "The solid particle erosion of metallic materials: the rationalization of the influence of material variables". In: *Wear* 186 (1995), pp. 129–144.

[77] G.P. Tilly. "A two stage mechanism of ductile erosion". In: *Wear* 23.1 (1973), pp. 87–96.

[78] E.T. Ulset. "Utilizing Solar Vapour Energy by Use of Nanofluids in a Direct Absorption Solar Collector". MA thesis. The University of Bergen, 2018.

[79] Det Norske Veritas. "Recommended practice RP O501 erosive wear in piping systems". In: *DNV Recommended Practice* 4 (2007).

[80] H.K. Versteeg and W. Malalasekera. *An introduction to computational fluid dynamics: the finite volume method*. Pearson education, 2007.

[81] M.H. Wang, C. Huang, K. Nandakumar, P. Minev, J. Luo, and S. Chiovelli. "Computational fluid dynamics modelling and experimental study of erosion in slurry jet flows". In: *International Journal of Computational Fluid Dynamics* 23.2 (2009), pp. 155–172.

[82] X. Wang, X. Xu, and S.U.S. Choi. "Thermal conductivity of nanoparticle-fluid mixture". In: *Journal of Thermophysics and Heat Transfer* 13.4 (1999), pp. 474–480.

[83] F.H. Wetzel. "The characterization of pressure-sensitive adhesives". In: *ASTM Bulletin* 221 (1957), pp. 64–68.

[84] S. Witharana, H. Chen, and Y. Ding. "Stability of nanofluids in quiescent and shear flow fields". In: *Nanoscale Research Letters* 6.1 (2011), pp. 1–6.

[85] H. Xie, J. Wang, T. Xi, Y. Liu, F. Ai, and Q. Wu. "Thermal conductivity enhancement of suspensions containing nanosized alumina particles". In: *Journal of Applied Physics* 91.7 (2002), pp. 4568–4572.

[86] Y. Xuan and Q. Li. "Heat transfer enhancement of nanofluids". In: *International Journal of Heat and Fluid Flow* 21.1 (2000), pp. 58–64.

[87] W. Yu and H. Xie. "A review on nanofluids: preparation, stability mechanisms, and applications". In: *Journal of Nanomaterials* 2012 (2012).

[88] Y. Zhang, E.P. Reuterfors, B.S. McLaury, S.A. Shirazi, and E.F. Rybicki. "Comparison of computed and measured particle velocities and erosion in water and air flows". In: *Wear* 263.1-6 (2007), pp. 330–338.

[89] H. Zhu, Y. Lin, and Y. Yin. "A novel one-step chemical method for preparation of copper nanofluids". In: *Journal of Colloid and Interface Science* 277.1 (2004), pp. 100–103.

Appendices

Appendix A

Mass Measurements of Target Samples

This appendix contains additional data of the target masses before and after the conducted erosion tests.

Table A.1: The weight of the material samples before and after tests

		Initial mass [g]	After first water-test [g]	09.03 [g]	05.05 [g]	06.05 [g]	07.05 [g]	07.05 [g] (after wood spirit)	08.06 [g] (after NF test)
Plastic	#1	1.7142	1.7441	1.7287	1.7934	1.7903	1.7857	1.7849	1.7805
	#2	1.7065	1.7361	1.7215	1.7645	1.7614	1.7585	1.7576	1.7527
	#3	1.7343	1.7637	1.7487	1.7725	1.7678	1.7647	1.7631	1.7558
Rubber	#1	1.5504	1.8453	1.7042	2.0467	1.9945	1.9613	1.9566	2.034
	#2	1.5439	1.8288	1.6909	2.0313	1.9929	1.961	1.9575	2.0284
	#3	1.5436	1.8393	1.6957	2.0383	1.9944	1.9663	1.9615	2.0188
Copper	#1	10.7144	10.7103	10.7103	10.3595	10.3595	10.359	10.3568	10.3494
	#2	10.5033	10.4972	10.497	10.4817	10.4817	10.4815	10.4809	10.4736
	#3	10.363	10.3582	10.358	10.7001	10.7002	10.6999	10.6996	10.6929